CFDRC
215 Wynn Drive • Huntsville, Alabama 35805
Tel.: (256) 726-4800 • FAX: (256) 726-4806
www.cfdrc.com • info@cfdrc.com

LES SOFTWARE FOR THE DESIGN OF LOW EMISSION COMBUSTION SYSTEMS FOR VISION 21 PLANTS

Quarterly Technical Progress Report for

January - March 2003

by

Steven Cannon
Clifford Smith

April 2003 **CFDRC Report No. 8321/10**

Contract No.: DE-FC26-00NT40975

submitted to

AAD Document Control, M/S 921-107
National Energy Technology Center
U.S. Department of Energy
P.O. Box 10940
Pittsburgh, PA 15236

Technical Monitor: Mr. Norman T. Holcombe
Contract Monitor: Ms. Crystal Sharp

DISCLAIMER

ABSTRACT

Application and testing of the new combustion Large Eddy Simulation (LES) code for the design of advanced gaseous combustion systems is described in this 10th quarterly report. CFD Research Corporation has developed the LES module within the parallel, unstructured solver included in the commercial CFD-ACE+ software. In this quarter, validation and testing of the combustion LES code was performed for the DOE-Simval combustor. Also, Beta testing by consortium members was performed for various burner and combustor configurations.

In the two quarters ahead, CFDRC will validate the code on the new DOE SimVal experiments. Experimental data from DOE should be available in June 2003, though LES calculations are currently being performed. This will ensure a truly predictive test of the software. CFDRC will also provide help to the consortium members on running their cases, and incorporate improvements to the software suggested by the beta testers. The beta testers will compare their predictions with experimental measurements and other numerical calculations. At the end of this project (October, 2003), a final released version of the software will be available for licensing to the general public.

TABLE OF CONTENTS

LIST OF FIGURES

LIST OF TABLES

1. INTRODUCTION

Vision 21 combustion systems will require innovative low emission designs and low development costs if Vision 21 goals are to be realized. In this three-year project, an advanced computational software tool will be developed for the design of low emission combustion systems required for Vision 21 clean energy plants. The combustion Large Eddy Simulation (LES) software will be able to accurately simulate the highly transient nature of gaseous-fueled turbulent combustion so that innovative concepts can be assessed and developed with fewer high-cost experimental tests. During the first year, the project included the development and implementation of improved chemistry (reduced GRI mechanism), subgrid turbulence (localized dynamic), and subgrid combustion-turbulence interaction (Linear Eddy) models into the CFD-ACE+ code. University expertise (Georgia Tech and UC Berkeley) has been utilized to help develop and implement these advanced submodels into the unstructured, parallel CFD flow solver. Efficient numerical algorithms that rely on *in situ* look-up tables or artificial neural networks have been implemented for chemistry calculations. In the second year, the combustion LES software has been evaluated and validated using experimental data from lab-scale and industrial test configurations. During the last year, nine industrial and academic partners will take the combustion LES code and exercise it on problems of their choice. Final feedback and optimizations will then be implemented in the final release version of the combustion LES software that will be licensed to the general public.

2. EXECUTIVE SUMMARY

Work in this tenth quarter (January - March 2003) has included further development of the LES software. Initial predictions have been performed for the DOE-SimVal lean premixed combustor. Beta testing from the gas turbine and industrial burner companies is also underway and initial results have been obtained.

Next quarter, completion of the following tasks are planned:

1. Perform DOE SimVal combustor predictions.

2. Support beta testers.

3. Implement LES software improvements based on beta testers feedback.

3. EXPERIMENTAL

No experiments were performed this quarter.

4. RESULTS

4.1 DOE-HAT Combustor Validation

DOE NETL has established a new experimental combustor design, called SimVal, that will be tested starting in June of 2003. The SimVal combustor will provide experimental data that can be used to validate CFD codes, with particular emphasis on understanding combustion instability and variable fuel effects at actual gas turbine combustor conditions. Detailed experimental data will be obtained, including emission images, velocity, temperature, and species maps, and dynamic wall pressure. Predictions are being performed now for later comparisons to data. A panel session, consisting of four commercial CFD software companies, will present SimVal combustor predictions at the IGTI ASME Gas Turbine Expo this summer. CFDRC, along with Fluent, Flow Parametrics, and CFX are participating in the panel session. The session chairs are Bob Malecki from Pratt & Whitney and Dan Maloney from DOE-NETL.

The current SimVal geometry includes a choke plate immediately upstream of swirl vanes and a choked nozzle at the downstream end of a resonant section. Figure 1 shows the current baseline geometry. The swirler (Figure 2) includes 32 thin slots with a 30° and significant blockage (0.286=flow area/total area). Bob Malecki performed cold-flow simulations of the swirler and produced the velocity profiles 2" from the combustor dump as shown in Figure 3. The swirl angle ranges from 55° to 65° in the annular injector passage. These profiles were applied as boundary conditions in the reacting case.

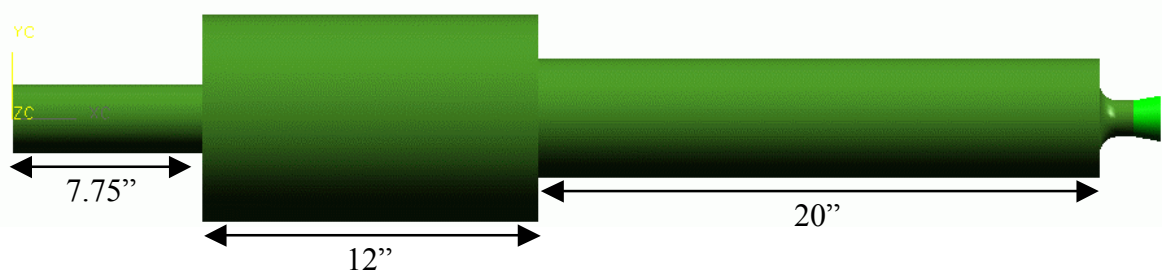

Figure 1. SimVal Geometry for Baseline Case

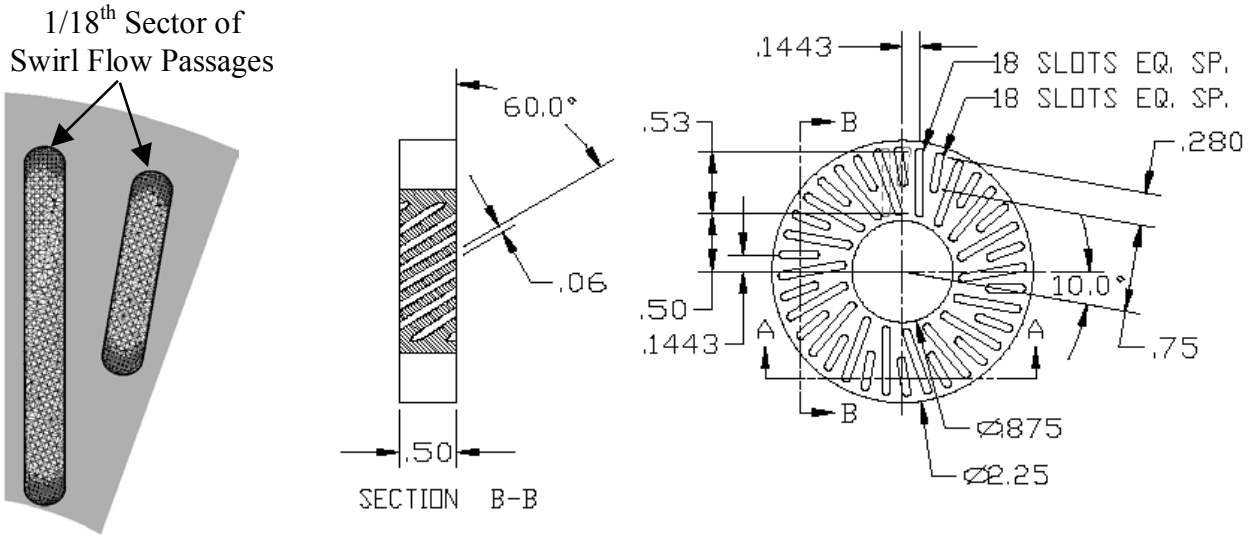

Figure 2. Schematic of Swirler Geometry

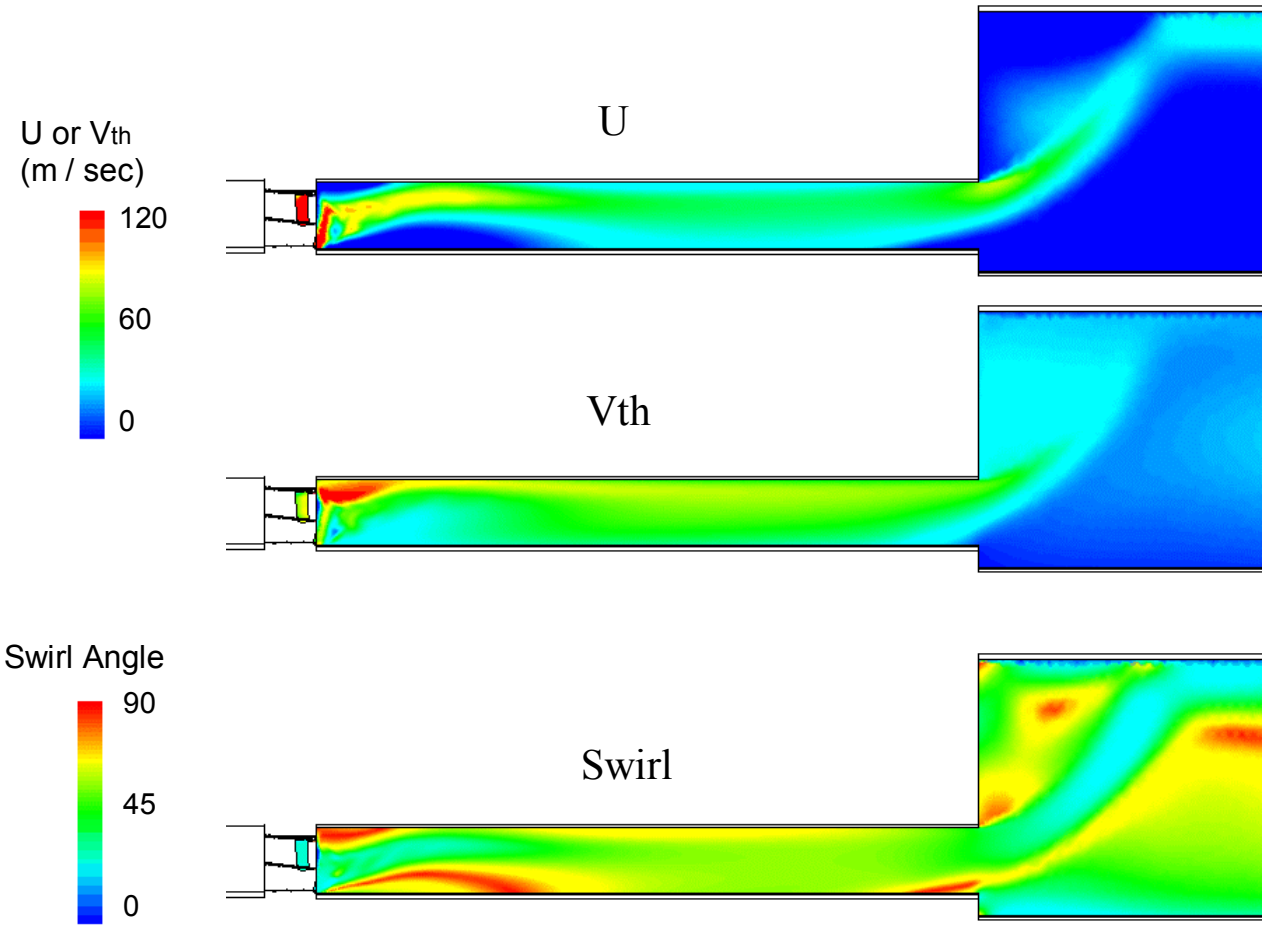

Figure 3. Predicted Velocity Profiles from 3D Swirler Simulation from P&W; Used for Inlet BCs

Initial 2D axisymmetric calculations have performed. The baseline case was simulated at the following conditions:

$\phi = 0.6$
Mass Flow = 0.26 kg/s
$T_{in} = 600$ K
P = 4 atm

A fixed mass flow with completely premixed reactants was assumed at the inlet. The fully burned conditions provided a choked flow at the nozzle throat with a combustor pressure of ~4 atm. An extrapolated boundary condition was used at the supersonic nozzle exit. The quartz combustor side walls were assumed to be 1650 K. The other combustor dome and resonant section walls were assumed to be 658 K. A wall temperature of 1144 K was assumed at the nozzle. Calculations were performed on the parallel Linux PC cluster using 4 processors.

A computational grid of ~15,000 cells was used. Turbulence and turbulence-chemistry interactions models included the RNG k-ε and 2-dimensional assumed PDF method, respectively. Steady-state predictions for the baseline case are shown in Figure 4. The steady results show the expected swirl stabilized flame with central and outer recirculation zones. The swirling flow attaches to the outer combustor wall before flowing out through the resonant section and into the choked nozzle. Combustor temperatures reach 1850 K and resonant section temperatures are around 1800 K. The NO_x emissions reach an exit value of around 10 ppm, while the CO oxidizes down to around 20 ppm.

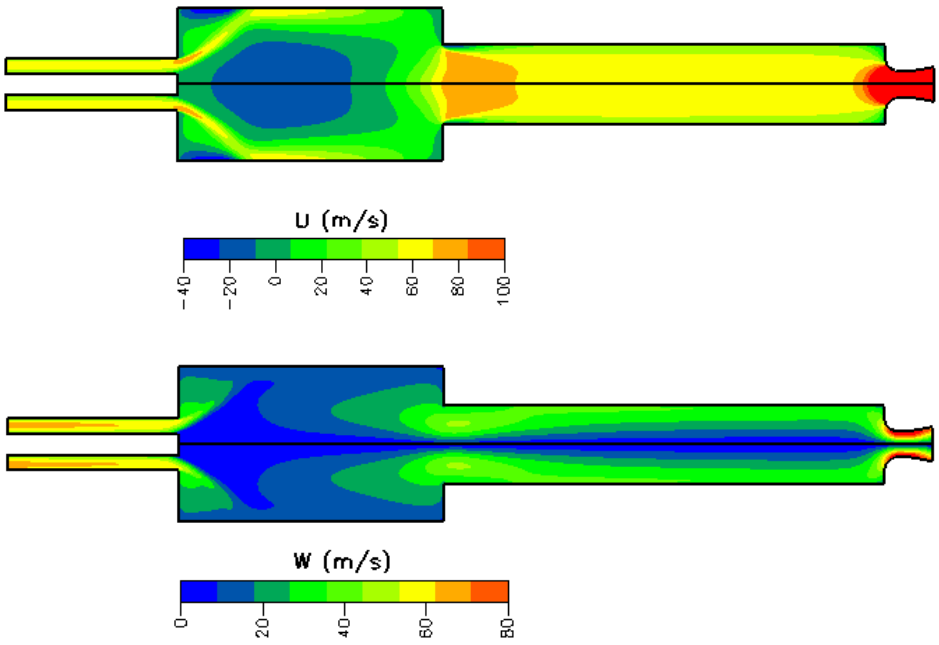

Figure 4. Steady-state Predictions of U-velocity, W-velocity, Temperature, Total Pressure, NO_x, and CO

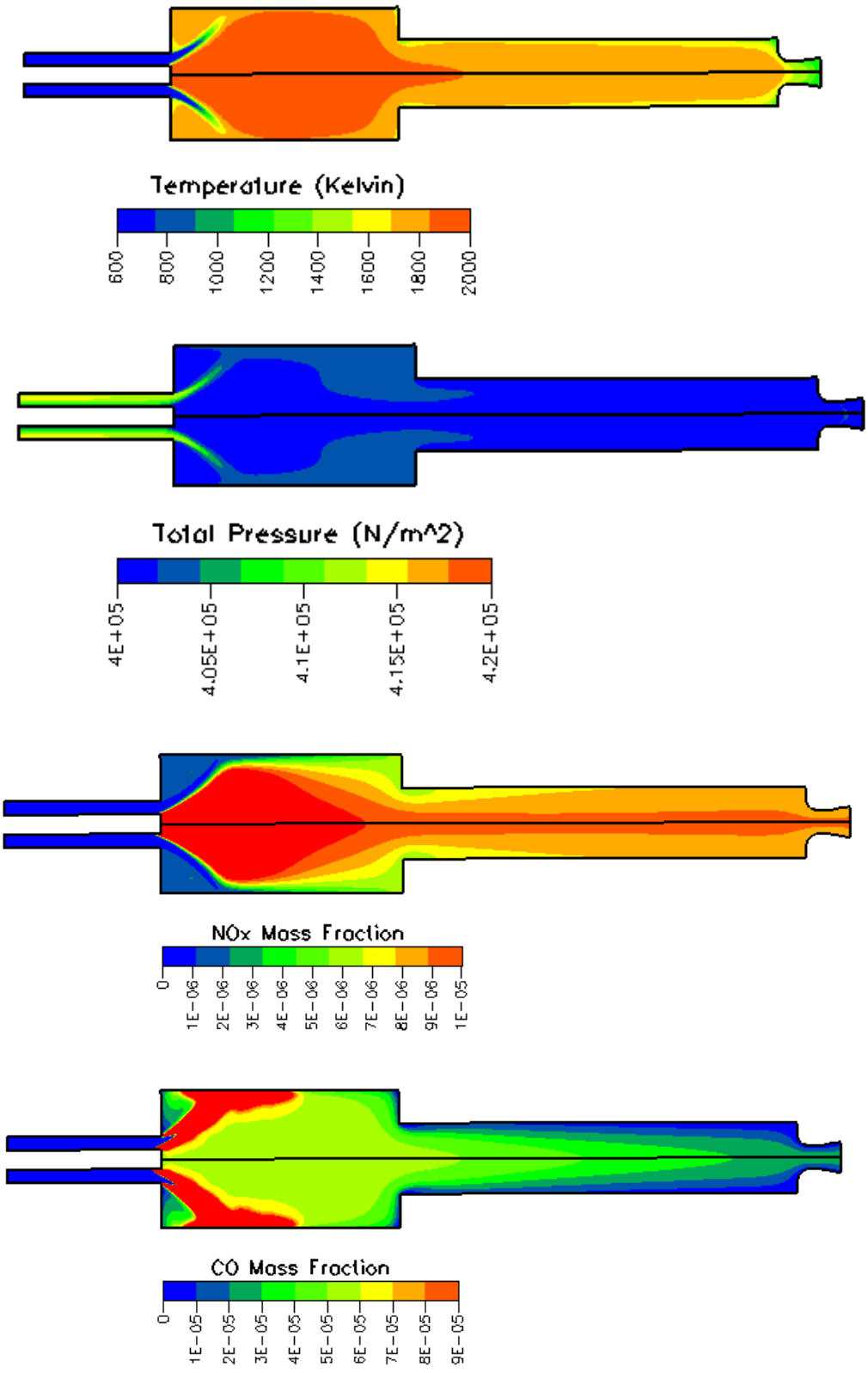

Figure 4 (concluded). Steady-state Predictions of U-velocity, W-velocity, Temperature, Total Pressure, NO_x, and CO

The unsteady RANS predictions were performed at a time-step of 5e-6 seconds. A predicted frequency of ~410 Hz was resolved, though at a relatively low level (~0.013% of mean pressure). Based on the unsteady RANS results, this combustor should be relatively quiet at these conditions. 3D LES calculations are now being set up and run, as well as predictions at other equivalence ratios (0.5, 0.7, and 0.8).

4.2 Initial Beta Test Results

Solar Turbines: Solar Turbines has been generating a grid for a premixer in an industrial lean premixed combustor. The grid was generated with the commercial package, Grid-Pro. Grid-Pro utilizes a smoothing algorithm that provides nearly orthogonal structured cells. Solar has found that Grid-Pro grids produce converged results almost 3 times faster than conventional non-orthogonal grids.

The premixer geometry includes an upstream plenum that feeds a swirler with downstream fuel spokes. The premixer annular passage then dumps into a combustor geometry. A 60 degree sector was modeled that included 1 swirl vane and two fuel spokes. Cyclic boundary conditions are needed for this configuration. It was found that Grid-Pro generates different numbers of face patches on each cyclic side of the geometry, even though a 1-to-1 cell match exists across the cyclic sides. Until now, CFD-ACE+ was restricted to have a 1-to-1 cell and face match. This restriction was eliminated in the SOLVER and GUI so that a 1-to-1 face match was not required.

Another hurdle came up as Solar tried to use the Grid-Pro grid. It was found that during merging of H-Grids, that Grid-Pro can sometimes create O-grids. CFD-ACE+ cannot handle O-grids, but can handle two C-grids that fill the same purpose of a single O-grid. This restriction required a limit of merging only up to 3 blocks at a time. This 3-block merging limit did not allow O-grids to form. It now appears that it should be possible to run CFD-ACE+ on the Solar Grid-Pro grid. The boundary conditions are now being set up and run at CFDRC, before turning over the case to Al Kubasco at Solar.

Rolls Royce: Rolls Royce has installed the CFD-ACE+ software at their Indianapolis site. Sunil James is now setting up a case for modeling the Sydney Swirl Burner. Results should be available in the next quarterly report.

Babcock & Wilcox: Alan Sayre at Babcock and Wilcox (B&W) has made good progress in setting up the parallel LES software and running an initial non-reacting Sandia/BERL furnace simulation. The furnace and burner geometry are shown in Figures 5 and 6. The 300 kW swirl-stabilized natural gas burner was designed and built by the International Flame Research Foundation (IFRF). The burner is circumferentially symmetric with a bluff center body containing 24 radial natural gas injection holes. Combustion air is supplied by a blower and introduced through the annular air zone and swirled using IFRF swirl blocks. The burner has the capability for flue gas recirculation (FGR) and fuel staging, but was operated only in the single-stage mode without FGR for the baseline validation case.

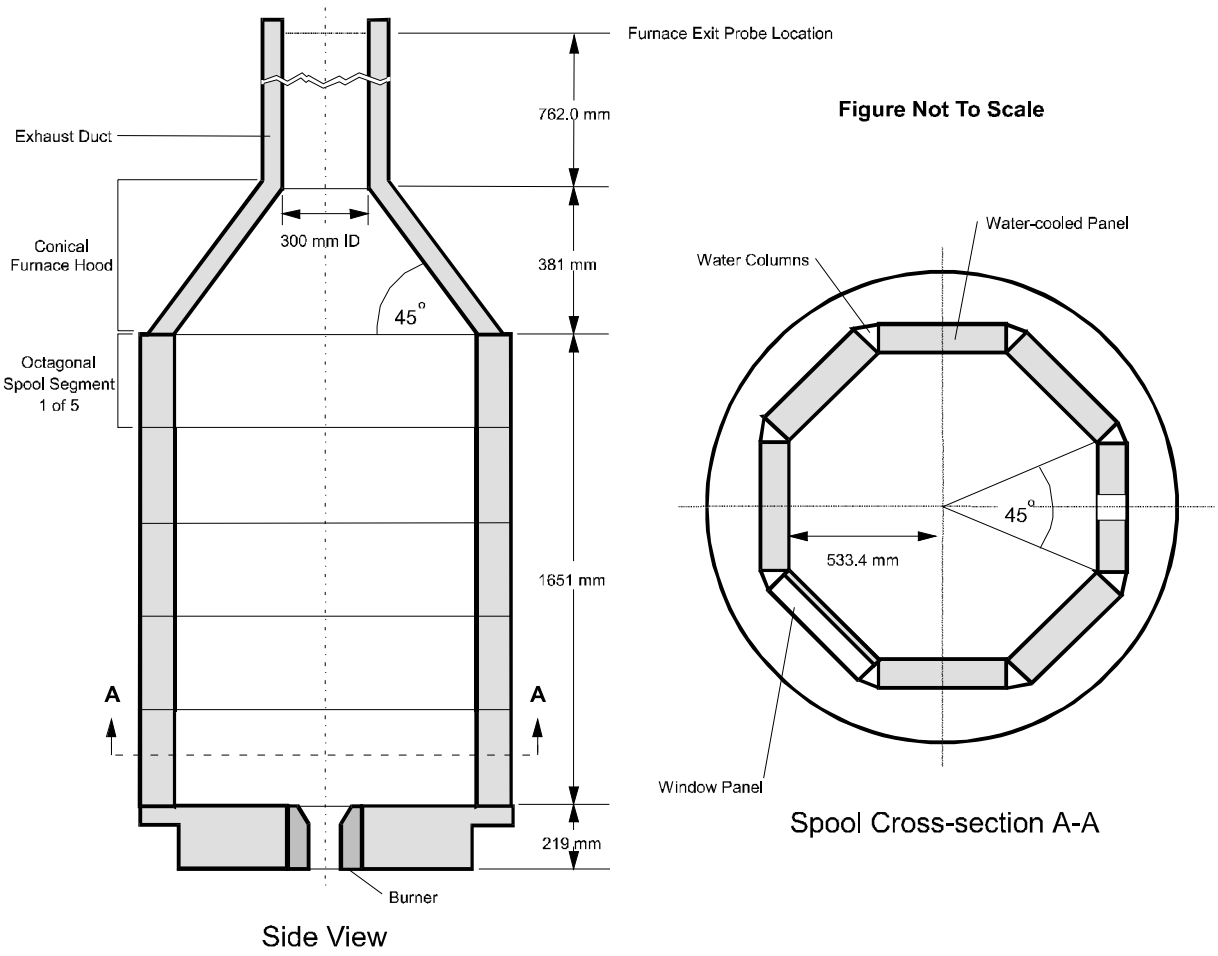

Figure 5. Schematic of BERL Furnace (Forniciari et al., 1994)

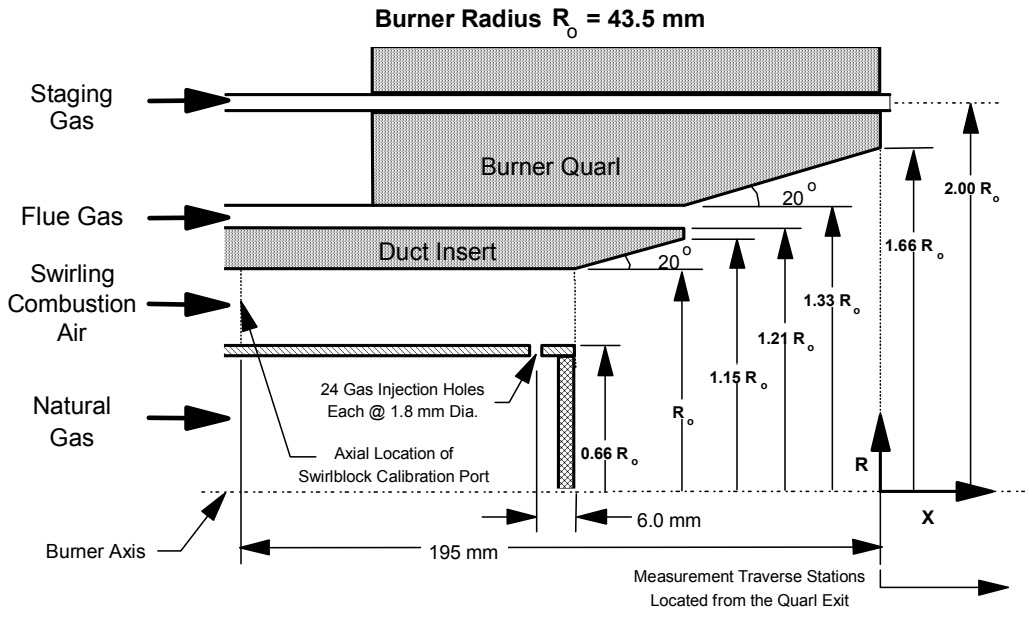

Figure 6. IFRF 300 kW Natural Gas Burner (Forniciari et al., 1994)

Tables 1 and 2 show the inlet combustor air and natural gas conditions for the baseline flame, low excess air flame, and cold-flow. A comprehensive set of spatially-resolved experimental data throughout the burner and furnace is available for CFD model validation, including: LDV for mean and RMS velocity and suction pyrometer for mean temperatures. Mean species compositions were measured with infrared (CO and CO_2), flame ionization (total hydrocarbons), paramagnetic (O_2), chemiluminescence (NO and NO_x), and micro-gas chromatograph (H_2, O_2, CO, CO_2, CH_4, and N_2).

Table 1. Burner Combustion Air Inlet Conditions

Condition	***Baseline Flame***	***Low Excess Air Flame***	***Cold Flow***
Date	1995.05.23	1995.06.09	1995.05.11
Ambient Pressure (kPa)	99.04	99.57	99.31
Mole Fraction H_2O (-)	0.0166	0.0134	0.0100
Gauge Pressure (kPa)	2.60	2.20	2.20
Air Temperature (K)	311.4	306.4	304.3
Molecular Weight	28.783	28.827	28.855
Density	1.1296	1.1523	1.1576
Air Flow (kg/s)	0.1194	0.1069	0.0867
Stoichiometric Ratio	1.15	1.033	N/A
	Inlet Area = $3.4331 \cdot 10^{-3}$		
	Swirl Number $S_2 = 0.56$		
Mean Axial Velocity (m/s)	30.79	27.02	29.36
Mean Tangential Vel. (m/s)	16.67	18.20	15.71
	Turbulence Intensity (%) = 13.51		
Suggested Turbulence Parameters:			
Turb. Kinetic Energy (J/kg)	33.56	29.06	30.36
	Characteristic Length = $7.6125 \cdot 10^{-3}$ m		
Dissipation Rate of Turb. Kinetic Energy ($J \cdot kg^{-1} \cdot s^{-1}$)	$5.995 \cdot 10^4$	$4.832 \cdot 10^4$	$5.158 \cdot 10^4$

Table 2. Burner Natural Gas Inlet Conditions

Condition	***Baseline Flame***	***Low Excess Air Flame***
Date	1995.05.23	1995.06.09
LHV (MJ/kg)	48.20	46.97
Stoichiometric Air/Fuel Ratio	16.75	16.28
Molecular Weight (kg/kmol)	17.12	17.12
Fuel Temperature (K)	312.0	310.8
Density (kg/m^3)	0.7318	0.7372
Gauge Pressure (kPa)	11.85	11.70
Fuel Flow (kg/s)	0.006229	0.006360
Mean Radial Velocity (m/s)	139.4	141.3
Suggested Turbulence Intensity (%)	5	5
Suggested Turbulence Parameters:		
Turb. Kinetic Energy (J/kg)	72.87	74.83
Characteristic Length = $0.9 \cdot 10^{-3}$ m		
Dissipation Rate of Turb. Kinetic Energy ($J \cdot kg^{-1} \cdot s^{-1}$)	$1.62 \cdot 10^6$	$1.69 \cdot 10^6$

Mie scattering images were collected for non-reacting and baseline reacting conditions. Figure 7 shows instantaneous snapshots of the flow structure entering the furnace. The closed internal recirculation zone for the baseline flame is visible, while an open recirculation zone is formed by the non-reacting flow. These images are useful in defining key mixing layers and structures that can be compared with LES predictions.

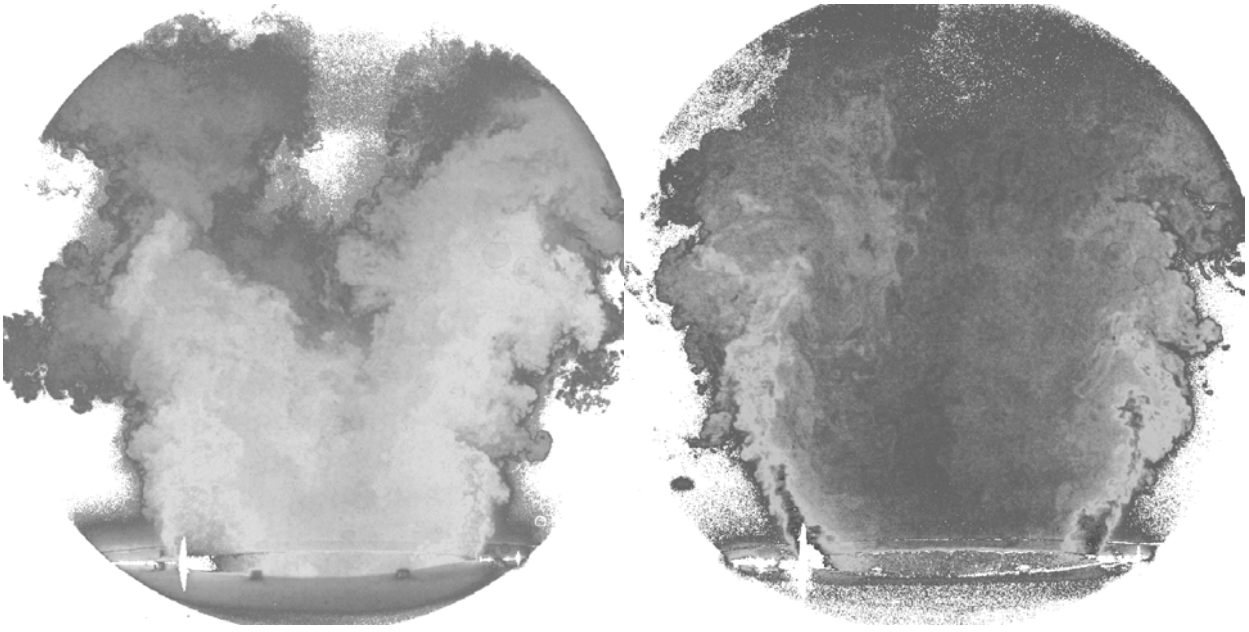

Figure 7. Mie Scattering Images for Non-Reacting and Baseline Reacting Conditions

B&W has an 8 PC Linux cluster for running the software. The computational grid of the BERL furnace was generated using CFD-GEOM. A 350,000 cell grid was used to represent a 45 degree sector of the swirl burner and furnace. Cyclic boundaries were used and the case was run in parallel on the 8 Pcs. Figure 8 shows the computational grid.

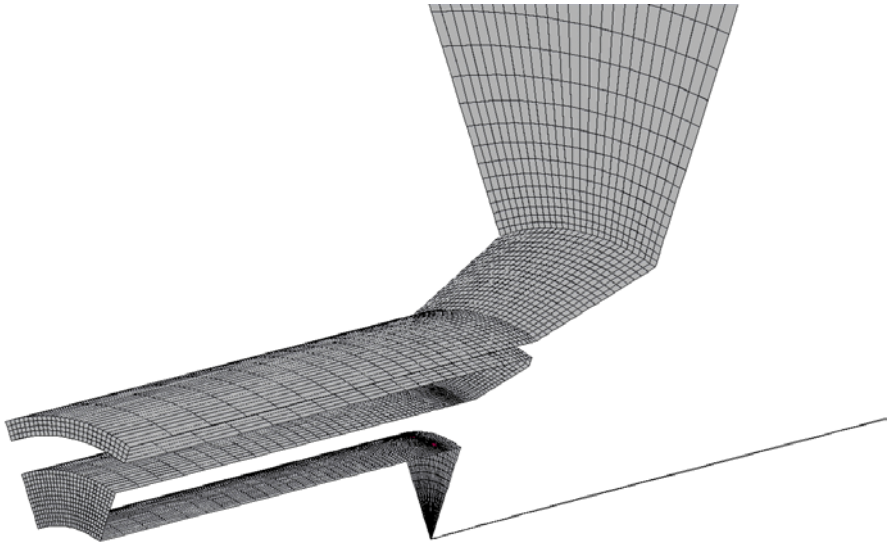

Figure 8. Computational Grid of the Burner Region for the B&W LES Furnace Simulation

Initial LES results were performed at a time-step of 1E-6 seconds and using the Localized Dynamic subgrid Kinetic energy Model (LDKM). Flowfield snapshots and monitor points throughout the flowfield showed that the instantaneous flowfield did not change from the time-averaged flowfield. Instabilities along shear layers were not formed. It was determined that a finer grid was needed, particularly in the initial shear layers near the furnace dump plane. It is anticipated that a 700,000 cell grid will be utilized for the next round of LES calculations.

Virginia Tech: Virginia Tech has set up and run 2d axisymmetric LES calculations of their swirl stabilized combustor using the CFD-ACE+ code. The combustor includes a lean premixed swirl injector with a round head bluffbody and a diverging conical section (quarl). The quarl is followed by a step that forms the combustor dump. Figure 9 shows a combustor schematic with central and outer recirculation zones that stabilize the flame.

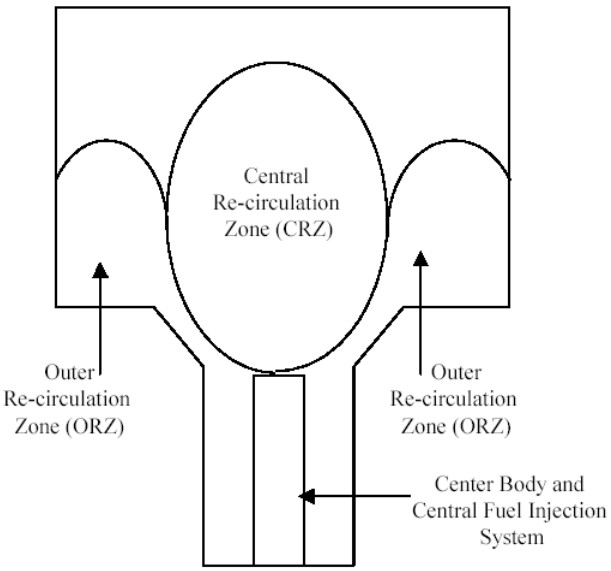

Figure 9. Schematic Showing Recirculation Zones in the Virginia Tech Swirl Stabilized Combustor

Boundary conditions for the model included measured mean and rms velocity profiles at the inlet (just downstream of the swirler). A premixed methane-air mixture with an equivalence ratio of 0.5 enters the combustor with a flow rate of 20 SCFM and a swirl number of 1.2. The actual swirl number used in the LES appears to be closer to 0.2 and so this will be corrected for reporting of future results. The 19-step reduced GRI mechanism was used along with the Linear Eddy model (LEM) for subgrid turbulence-chemistry interactions. The LDKM was applied for modeling subgrid turbulence. The combustor walls, made of quartz glass, were assumed to be adiabatic.

The experimentally measured frequency response function (FRF) between the OH chemiluminescence and the incoming mass flow fluctuations is shown in Figure 10. As can be observed, a large amplitude 200 Hz oscillation appears, as well as some preferred frequencies between 250 and 500 Hz. These frequencies have not yet been explained for the experimental data.

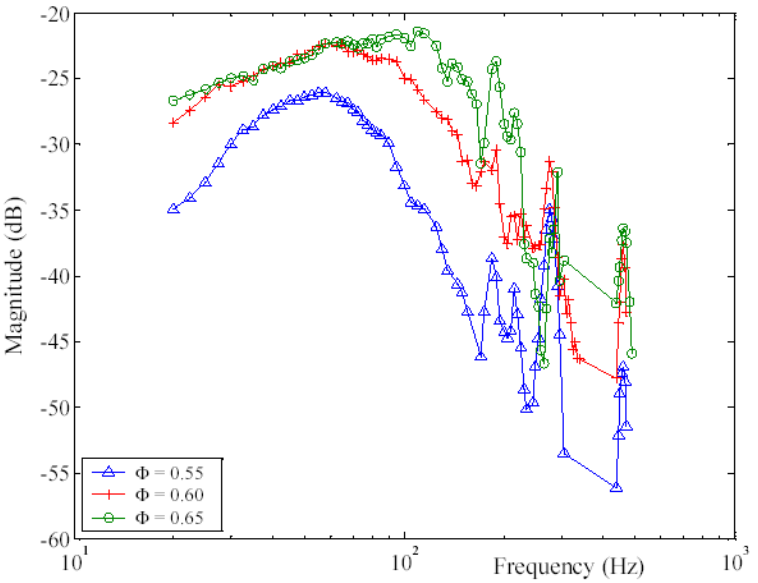

Figure 10. Measured Magnitude of Frequency Response Function (FRF) Between OH Heat Release Rate and Inflow Velocity*

Figures 11 and 12 show results for the LES. The temperature PSD plot represents a monitor point at the dump plane of the combustor. A strong 220 Hz frequency is observed, in agreement with measured frequencies. The temperature flowfield snapshots indicate that vortex shedding near 220 Hz is occurring and could be the cause of the measured dynamics. Further work is being done to correct the swirl velocity at the inlet and to compare the CFD results with the experimental data (steady and time-varying temperature measurements and FRF data). Also, a full 3D computation of the reacting flowfield will be carried out.

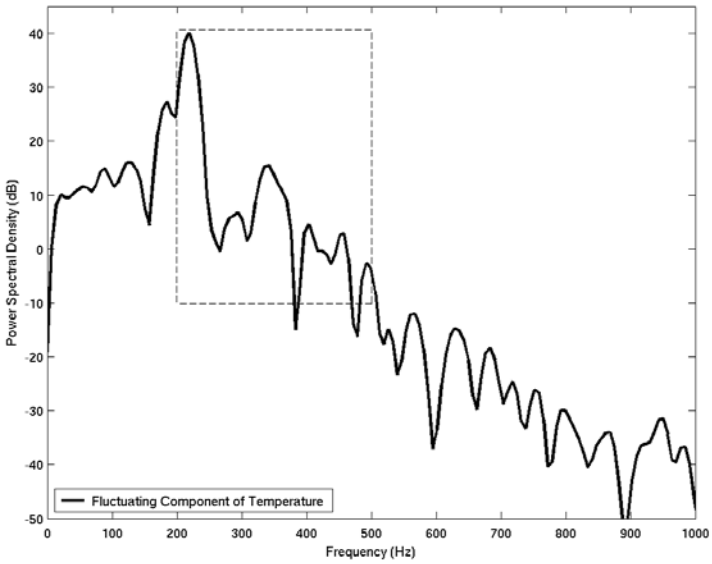

Figure 11. LES Predicted Power Spectral Density (PSD) of Fluctuating Component of Temperature at Combustor Dump Plane

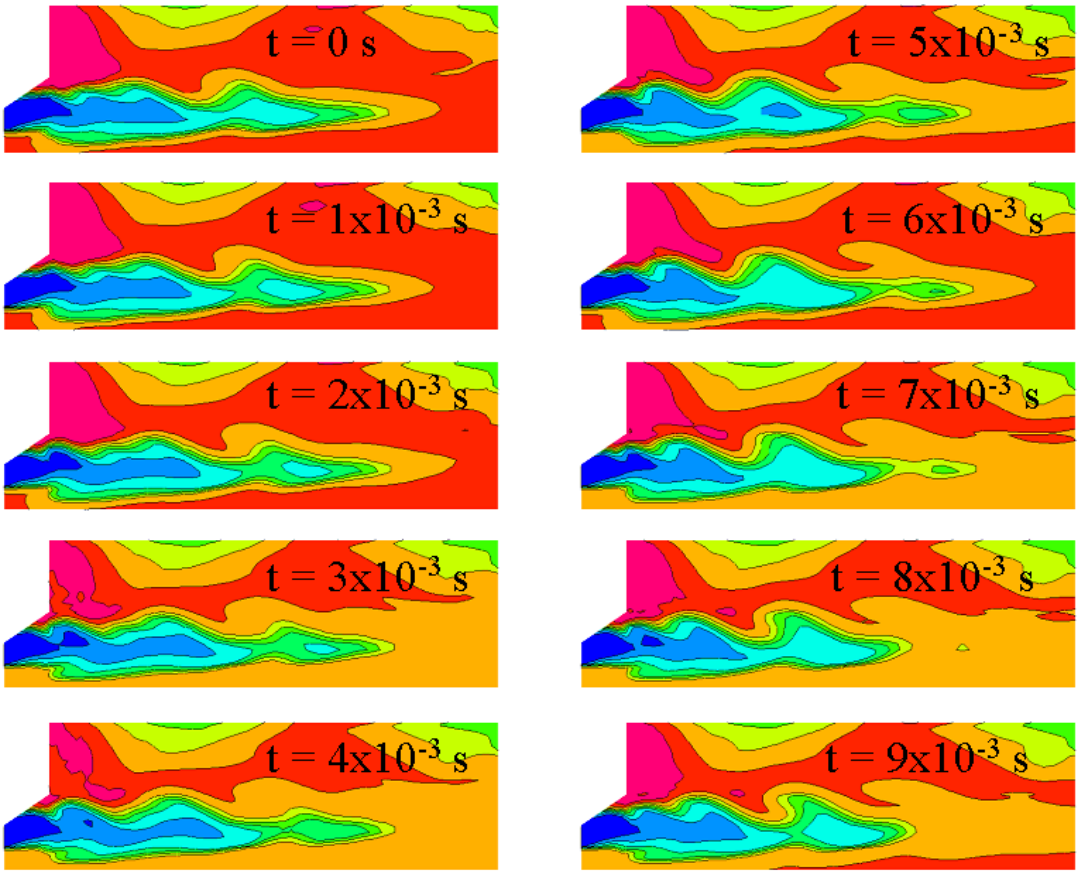

Figure 12. LES Predicted Temperature Contours Showing Unsteady Behavior of Flame

Coen: Paul Matys at Coen has recently set up a cluster of 16 Linux Pcs and has installed the CFD-ACE+ software. Coen will run a bluff-body stabilized flame for evaluating the LES software. LES predictions with the new CFD-ACE+ software will be compared with Fluent and with experimental data. These results should be available in the next quarter.

4.3 Georgia Tech LES of DOE-HAT Combustor

Georgia Tech has carried out 3D LES of the DOE-HAT combustor. The LDKM model, as implemented in CFD-ACE+, was used to represent the subgrid turbulent stresses. A thin-flame turbulent propagation model was combined with a mixture fraction based flamelet library to predict the turbulence-chemistry interactions. They obtained excellent agreement with measurements for CO and NOx emissions as a function of equivalence ratio. The LES predicted the observed increase in CO emissions as lean blowout was approached. Results from this work are included in Appendix C.

5. CONCLUSIONS

The combustion LES code is being tested by the industrial and academic consortium members. Initial feedback has indicated a need for easily generating a fine-enough grid for LES resolution. Also, modifications for handling Grid-Pro grids have been implemented based on user feedback. Further validation of the code at CFDRC is being performed on the DOE-SimVal combustor. 3D LES predictions of the DOE-HAT combustor were also performed by Georgia Tech. Good agreement with CO and NO_x emissions was obtained.

6. REFERENCE

Fornaciari, N., Schefer, R., Paul, P., Sanford, R., Claytor, L., and Lubeck, C., 1994, "Users Guide to the Burner Engineering Research Laboratory," Presented to the American Flame Research Committee/Japanese Research Committee at the Pacific Rim International Conference on Environmental Control of Combustion Processes, October 16-20, Maui, Hawaii.

APPENDIX A — WORK SCHEDULE

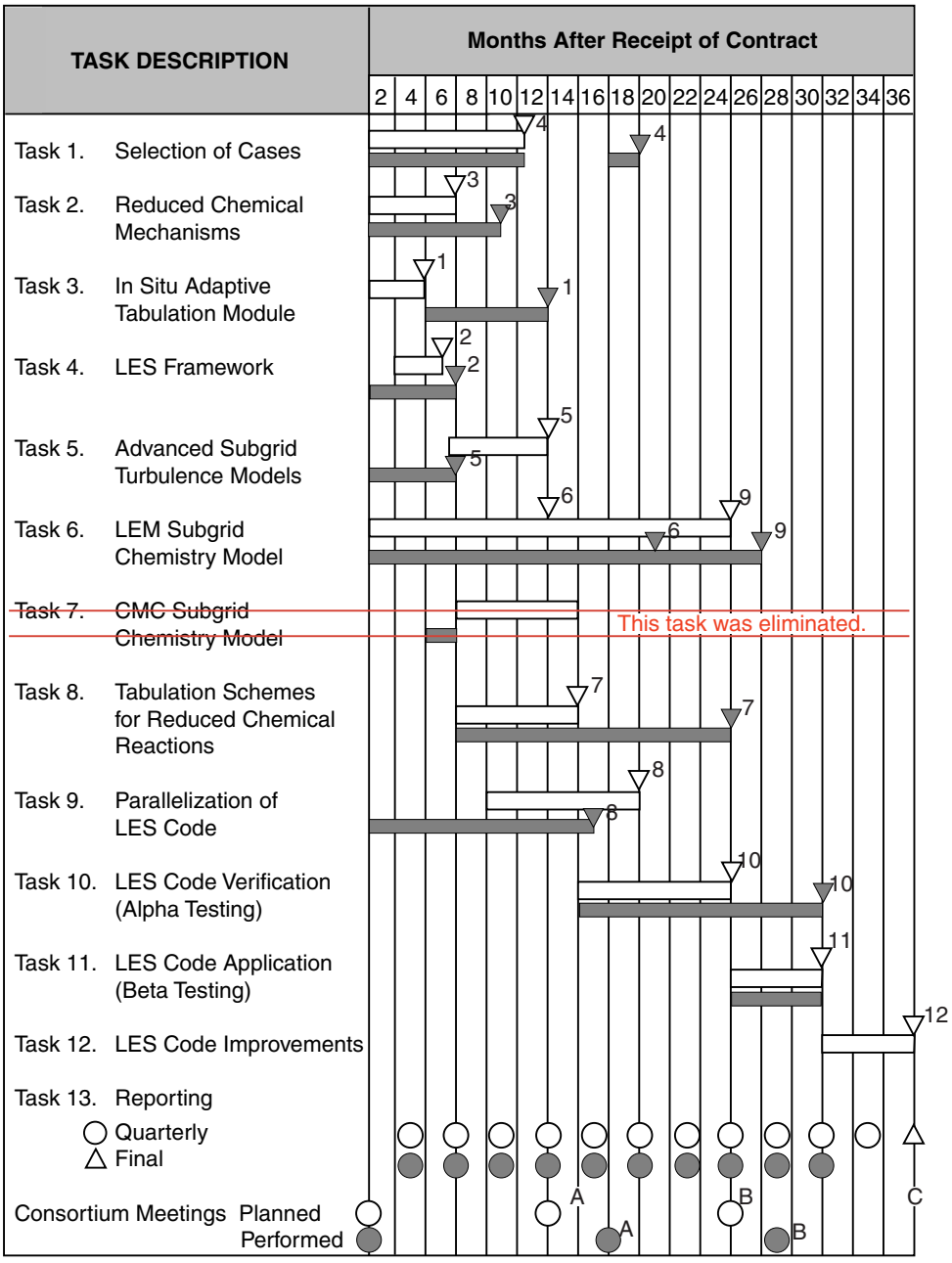

Key Milestones

1 Complete In-Situ Adaptive Tabulation Module
2 Complete LES Framework Modification to CFD-ACE+
3 Complete Reduced Mechanisms
4 Complete Selection of Cases
5 Complete Implementation of Turbulence Models
6 Complete Implementation of Initial Version of LEM Model
7 Complete Tabulation Schemes
8 Complete Parallelization of LES Code
9 Complete Implementation of LEM Model
10 Complete Alpha Testing of LES Code
11 Complete Beta Testing of LES Code
12 Final Release of LES Code

Performance Targets

A Alpha Release of LES Code
B Beta Release of LES Code
C Final Commercial Release of LES Code

Planned
Performed

APPENDIX B — FUTURE PLANS

During the next quarter, the following work is planned:

1. Support beta testers.

2. Continue CFDRC validation of LES code for predicting emissions and instability of DOE SimVal experiment.

APPENDIX C — GEORGIA TECH LES OF DOE-HAT COMBUSTOR

Large-Eddy Simulation of Pollutant Emission in a DOE-HAT Combustor

G. Eggenspieler and S. Menon
School of Aerospace Engineering
Georgia Institute of Technology
ATLANTA, GA

May 2, 2003

Quarterly Report For Project E-16-T04
Submitted to
CFD Research Corporation

Abstract

Large-eddy simulation (LES) of turbulent premixed reacting flow in a DOE-HAT gas turbine combustor has been carried out to evaluate the use of LES to study combustion dynamics and to predict pollutant emission as lean-blow out (LBO) is approached. A localized dynamic model for the subgrid turbulent kinetic energy is used to close the subgrid stresses and heat flux in the LES equations, and a thin-flame turbulent propagation model is combined with a mixture fraction based flamelet library to predict the turbulence-chemistry interactions. Production of pollutants such as oxides of nitrogen (NO_x) and carbon monoxide (CO) is predicted using this model and compared to experimental data. Excellent agreement is obtained for CO and NO_x emission as a function of equivalence ratio, and the simulations predict the observed increase in CO emission as LBO is approached. Simulations also show that the dynamical (unsteady) interactions increase in intensity as LBO is approached.

1 Introduction

Recent more stringent emission regulations are pushing for the development of more fuel efficient and low-NO_x gas turbine systems. Hence, design studies of new devices will require accurate emissions prediction (CO, NO and unburnt hydrocarbons ,UHC) as a function of the operating conditions. Recent measurements in a full-scale combustor (denoted DOE-HAT, hereafter)[1] showed that, as the equivalence ratio is decreased, the CO emission first decreases and then, suddenly increases exponentially. This phenomenon (which is also observed in many other liquid- and gaseous-fueled gas turbine combustors) may (in some cases) be followed by, or related to, combustion instability during which the flame undergoes rapid oscillations and eventual blows out. This process is often called lean-blow out (LBO) and understanding and predicting this phenomenon is a major research issue and of serious concern for the industry. Past studies using RANS models[1] have been unable to capture this trend. More recently, a modified RANS approach using a flamelet model has been carried out at GEAEC[2–4] where good agreement with experimental data for the pollutant emission was demonstrated for a GE LM6000. However, the details of the combustion dynamics was not obtained since these studies did not account for the unsteady processes.

In the present effort, a new LES model is developed to study LBO in premixed combustion systems. The methodology follows closely the earlier study using the flamelet approach,[2,4] however, all closure issues are revisited within the LES subgrid formulation.

This paper is organized as follows. In the next section, the LES equations, the various closure issues and subgrid models are discussed . This is followed in Section 3 by the formulation of the flamelet approach, as implemented here. In Section 4, the current numerical method is summarized and then, the results of the current study are discussed in Section 5.

2 LES Model Formulation

2.1 LES equations

The governing equations of motion for an unsteady, compressible, reacting, multi-species fluid are the Navier-Stokes equations describing the conservation of mass, momentum, total energy and N-species. We employ the fully compressible version in this study since we are interested in the non-linear coupling between acoustic wave motion, vorticity dynamics and combustion heat release. In the LES methodology, the large scale motion is fully resolved on the computational grid using a time- and space-accurate scheme and only the small scales are modeled. The separation between the large (resolved) and the small (unresolved) scales is determined by the grid size ($\overline{\Delta}$). A Favre spatial top-hat filter (which is appropriate for the finite-volume scheme employed here) is employed to derive the LES equations.[5] Thus, any variable (f) is decomposed into a resolved quantity ($\widetilde{f}$) and a unresolved quantity (f'') such that $f = \widetilde{f} + f''$. The filtered Navier-Stockes equation (or the LES governing equations) are:[6]

$$\begin{cases} \frac{\partial \overline{\rho}}{\partial t} + \frac{\partial \overline{\rho}\widetilde{u_i}}{\partial x_i} = 0 \\ \frac{\partial \overline{\rho}\widetilde{u_i}}{\partial t} + \frac{\partial}{\partial x_j}\Big[\overline{\rho}\widetilde{u_i}\widetilde{u_j} + \overline{p}\delta_{ij} - \overline{\tau_{ij}} + \tau_{ij}^{sgs}\Big] = 0 \\ \frac{\partial \overline{\rho}\widetilde{E}}{\partial t} + \frac{\partial}{\partial x_i}\Big[\Big(\overline{\rho}\widetilde{E} + \overline{p}\Big)\widetilde{u_i} + \overline{q_i} - \widetilde{u_j}\overline{\tau_{ji}} + H_i^{sgs} + \sigma_i^{sgs}\Big] = 0 \\ \frac{\partial \overline{\rho}\widetilde{Y_m}}{\partial t} + \frac{\partial}{\partial x_j}\Big[\overline{\rho}\widetilde{Y_m}\widetilde{u_j} - \overline{\rho}\overline{D_m}\frac{\partial \widetilde{Y_m}}{\partial x_j} + \Phi_{j,m}^{sgs} + \Theta_{jm}^{sgs}\Big] = \overline{\rho}\widetilde{\dot{w}}_m, m = 1, N \end{cases} \quad (1)$$

In the above equations, u_i is the i-th velocity component, ρ is the mass density, p is the pressure and $E = e + \frac{1}{2}(u_k^2 + k^{sgs})$ is the total energy. Here, e is the internal energy per unit mass computed as the sum of the sensible enthalpy and the chemical stored energy, and k^{sgs} is the subgrid kinetic energy (defined below). Also, q_i is the heat flux vector and τ_{ij} is the viscous stress tensor, given by $\tau_{ij} = \mu\Big(\partial u_i/\partial x_j + \partial u_j/\partial x_i\Big) - \frac{2}{3}\mu\Big(\partial u_k/\partial x_k\Big)\delta_{ij}$. Here, μ is the molecular viscosity coefficient which is determined using the Sutherland's law. Finally, Y_i is the i^{th} species mass fraction and the molecular diffusion velocity $V_{j,m}$ is computed using the Fick's diffusion law with a constant diffusion coefficient (D_m): $V_{j,m} = -D_m\Big(\partial Y_m/\partial x_j\Big)$.

In the LES equations, all the above variables appear in their filtered form and many of these terms require closure. Some simplifications are required as well; for example, the filtered viscous shear stress ($\overline{\tau_{ij}}$) and heat flux ($\overline{q_i}$) are approximated using the filtered velocity and temperature . The subgrid terms in the equations represent the effect of the unresolved motion on the resolved field, and are: τ_{ij}^{sgs}, H_i^{sgs}, σ_i^{sgs}, $\Phi_{j,m}^{sgs}$ and Θ_{jm}^{sgs}. These terms are respectively, the subgrid shear stress, subgrid heat flux, subgrid viscous stress, subgrid mass flux and subgrid diffusive mass flux, and are defined as follows:

$$\begin{cases} \tau_{ij}^{sgs} = \overline{\rho}\Big[\widetilde{u_i u_j} - \widetilde{u_i}\widetilde{u_j}\Big] \\ H_i^{sgs} = \overline{\rho}\Big[\widetilde{E u_i} - \widetilde{E}\widetilde{u_i}\Big] + \Big[\overline{p u_i} - \overline{p}\widetilde{u_i}\Big] \\ \sigma_i^{sgs} = \overline{u_j \tau_{ji}} - \widetilde{u_j}\overline{\tau_{ji}} \\ \Phi_{jm}^{sgs} = \overline{\rho}\Big[\widetilde{Y_m u_j} - \widetilde{Y_m}\widetilde{u_j}\Big] \\ \Theta_{jm}^{sgs} = \overline{\rho}\Big[\widetilde{Y_m V_{j,m}} - \widetilde{Y_m}\widetilde{V_{j,m}}\Big] \end{cases} \quad (2)$$

2.2 Subgrid Closure of the LES Equations

In general, since the small-scales primarily provide dissipation for the energy that cascades from the large scales through the inertial range, an eddy viscosity type subgrid model appears appropriate to model the subgrid stresses τ_{ij}^{sgs},the heat flux H_i^{sgs} and the species flux Φ_{jm}^{sgs}. Assuming that an eddy viscosity ν_T can be prescribed, these subgrid fluxes can be approximated as:

$$\begin{cases} \tau_{ij}^{sgs} = -\nu_T\Big(\frac{\partial \widetilde{u_i}}{\partial x_j} + \frac{\partial \widetilde{u_j}}{\partial x_i}\Big) \\ H_i^{sgs} = -\nu_T\frac{\partial \widetilde{h}}{\partial x_i} \\ \Phi_{jm}^{sgs} = -D_T\Big(\frac{\partial \widetilde{Y_m}}{\partial x_j}\Big) \end{cases} \quad (3)$$

Here, $\widetilde{h}$ is the specific enthalpy and $D_T = \nu_T/Sc_t$ is the eddy diffusivity obtained in terms of the eddy viscosity and a turbulent Schmidt number Sc_t (assumed to be unity

here). The subgrid diffusive mass flux (Θ_{jm}^{sgs}) is neglected in this study, and the closure for the subgrid viscous stress σ_i^{sgs} is expected to be negligible.[7] Finally, the closures of the filtered reaction rate $\widetilde{\dot{w}}_m$ is described in section 3.

The subgrid viscosity ν_T is derived from the subgrid turbulent kinetic equation k^{sgs}. The k^{sgs} transport model is given as:

$$\frac{\partial \overline{\rho} k^{sgs}}{\partial t} + \frac{\partial}{\partial x_i}\Big(\overline{\rho}\widetilde{u_i} k^{sgs}\Big) = P^{sgs} - D^{sgs} + \frac{\partial}{\partial x_i}\Big(\frac{\overline{\rho}\nu_T}{Pr_T}\frac{\partial k^{sgs}}{\partial x_i}\Big) \tag{4}$$

Here, the subgird kinetic energy is defined as $k^{sgs} = \frac{1}{2}\Big[\widetilde{u_k^2} - \widetilde{u_k}^2\Big]$, and Pr_T is a subgrid Prandtl number, assumed to be unity.

In the above equation, P^{sgs} and D^{sgs} represent respectively, the production and dissipation of the subgrid kinetic energy. These terms are modeled as follow: P^{sgs} $= -\tau_{ij}^{sgs}\partial\widetilde{u_i}/\partial x_j$ and D^{sgs}=$C_\epsilon\overline{\rho}(k^{sgs})^{3/2}/\overline{\Delta}$. The subgrid stress is then obtained as: τ_{ij}^{sgs}= $-2\overline{\rho}\nu_T\Big(\widetilde{S_{ij}} - \frac{1}{3}\widetilde{S_{kk}}\delta_{ij}\Big) + \frac{2}{3}\overline{\rho}k^{sgs}\delta_{ij}$ where the subgrid eddy viscosity is given by: ν_T= $C_\nu(k^{sgs})^{1/2}\overline{\Delta}$

In the above equation, two model coefficients C_ϵ and C_ν appear and they must be prescribed or obtained dynamically as a part of the solution. Earlier studies[6, 8, 9] established a localized dynamic scale-similarity approach that did not employ the Germano's identity. This approach resulted in a robust and stable approach for determining the model coefficients locally in the combustor without requiring any averaging or smoothing. In the present study, we employ constant values of $C_\nu = 0.067$ and $C_\epsilon = 0.916$ that were established earlier using theoretical and numerical studies of high-Re stagnation point premixed flames.[10, 11] Localized dynamic evaluation of the model coefficients will be considered in the near future but the results reported here are not expected to be very sensitive to this issue.

3 Combustion and Heat Release Models

A thin-flame propagation model is employed here to resolve the flame in the flamelet burning regime. In this regime, the flame thickness (δ_L) is smaller than the smallest length scale (Kolmogorov scale η) and the burning time scale (τ_c) is smaller than the characteristic flow time (τ_f). This is generally the case in gas turbine combustion chamber. In this case, the thin laminar flame is wrinkled by the turbulent eddies, thereby increasing the instantaneous flame surface and hence, the effective burning or consumption rate. However, since even the smallest eddies are larger than the flame thickness they cannot penetrate into the flame and thus, the local burning speed is still equal to the laminar flame speed S_L. This approximation implies that classical methods to compute the laminar flame properties, such as the CHEMKIN program[12] can be used effectively.

It is noteworthy that although flamelet burning is prevalent in gas turbine combustors, there are also local regimes where the turbulence levels are so high that the smallest eddy is smaller than the flame thickness. This regime of burning is called distributed reaction zone or thin reaction zone[13] and in this regime, the smaller eddies penetrate into the flame zone thereby, thickening the flame. However, past studies have shown that even in this regime, the reaction zone is very thin and hence, flamelet burning approximation can still be employed. Models that explicitly account for flame broadening effect in the thin-reaction zone regime have also been developed.[9]

Two features are unique to this approach. The flame propagation model is based on the G-equation approach used in LES studies[6,9] and the turbulent burning speed is determined as a function of subgrid effects and laminar flamelet burning speed. The details of this approach are summarized below.

3.1 Flame Propagation

In the model employed here, the flame front is tracked as a infinitely thin surface that is convected by the flow and also propagates normal to itself at a characteristic flame speed S_F. The governing equation for this progress variable is based on the G-equation model:[14]

$$\frac{\partial \rho G}{\partial t} + \frac{\partial}{\partial x_i}\Big(\rho u_i G\Big) = -\rho S_F |\nabla G| \tag{5}$$

Here, G is a progress variable that has no physical meaning but it defines an infinitely thin level surface that separates $G = 1$ representing premixed fuel and $G = 0$ representing the burnt products. In laminar flow, $S_F = S_L$ which is the laminar burning speed. This speed contains the effect of the entire thermo-chemical state of the fuel-air mixture. Thus, for a given equivalence ratio S_L is uniquely defined.

By filtering this equation using the LES filter described in Section 2.2 LES version of the G-equation is obtained:

$$\frac{\partial \bar{\rho}\widetilde{G}}{\partial t} + \frac{\partial}{\partial x_i}\Big(\overline{\rho}\widetilde{u_i}\widetilde{G}\Big) = -\frac{\partial}{\partial x_i}\overline{\rho}\Big(\widetilde{u_i G} - \widetilde{u_i}\widetilde{G}\Big) - \overline{\rho S_F |\nabla G|} \tag{6}$$

Here $\widetilde{G}$ represents the effective flame brush thickness. This is in contrast to the original "laminar" interpretation of the G field where $G = 0$ denotes burned product and $G = 1$ denotes reactants, and the flame is considered an infinitely thin interface between $G = 0$ and $G = 1$. In the LES implementation, the filtered $\widetilde{G}$ represents the resolved flame brush which is an average location of the instantaneous thin flame.

The right hand side of Eq. (6) needs to be modeled. The subgrid convection term is modeled using a gradient assumption that incorporates the effect of the curvature of the flame as:[13]

$$-\frac{\partial}{\partial x_i}\Big(\widetilde{u_i G} - \widetilde{u_i}\widetilde{G}\Big) = -\overline{\rho} D_T \widetilde{\kappa} |\nabla \widetilde{G}| \tag{7}$$

where $\widetilde{\kappa}$ is the flame curvature defined as $\widetilde{\kappa} = \nabla \mathbf{n}$ where $\mathbf{n}$=$\nabla\widetilde{G}/|\nabla\widetilde{G}|$. Here, $\mathbf{n}$ is the unit normal oriented in the direction of flame propagation.

The flame front propagation term $\overline{\rho S_F |\nabla G|}$ is closed using a characteristic flame speed model. Thus, closed LES equation for the filtered progress variable $\widetilde{G}$ is:

$$\frac{\partial \bar{\rho}\widetilde{G}}{\partial t} + \frac{\partial}{\partial x_i}\Big(\overline{\rho}\widetilde{u_i}\widetilde{G}\Big) = -\overline{\rho} S_F^* |\nabla \widetilde{G}| - \overline{\rho} D_T \widetilde{\kappa} |\nabla \widetilde{G}| \tag{8}$$

where the effective burning speed in a turbulent flow S_F^* is a function of the laminar flame speed S_L and the subgrid turbulence intensity $u^{'}$.

3.2 Laminar Burning Speed

To obtain the laminar burning rate S_L, the detailed chemical kinetics occurring in the flame have to be properly estimated. Here, we employ a flamelet library approach since it is computationally efficient. In the flamelet library approach, the local chemical state is related to the mixture fraction $\widetilde{Z}$ which is obtained as the solution of a transport equation along with the LES equations. The influence of the subgrid turbulence upon the mixture fraction is included by solving another equation for the variance of the mixture fraction ($\widetilde{Z''^2}$). A simplified 1D problem is solved using detailed kinetics, the major species and the laminar burning rate S_L are tabulated as a function of $\widetilde{Z}$ and $\widetilde{Z''^2}$, and then retrieved during the actual LES.

It is clear that this approach substantially reduces the total cost of the simulation since chemical species are not tracked in the LES, and the stiffness of the chemical source terms is avoided. On the other hand, there are also some limitations. The flow must be such that a mixture fraction can be uniquely defined. Equal diffusivity for all species is implicitly assumed in the flow field since the mixture fraction is the only unknown variable (note that, during the flamelet library generation, detailed multi-component diffusion can be included but its effect on the actual flow field, and especially radicals, cannot be included directly in the mixture fraction formulation). Additionally, the formation of the pollutant species, especially in the post flame zone, cannot be accounted by this method, and the resolution of this problem will require new models, as to be described below.

The governing LES equation for the filtered mixture fraction used in this study is:

$$\frac{\partial \overline{\rho}\widetilde{Z}}{\partial t} + \frac{\partial}{\partial x_i}\left(\overline{\rho}\widetilde{u_i}\widetilde{Z}\right) = \frac{\partial}{\partial x_i}\left((D + D_T)\overline{\rho}\frac{\partial \widetilde{Z}}{\partial x_i}\right) \tag{9}$$

Here D is the molecular diffusivity and D_T is the subgrid turbulent diffusivity. Both D and D_T are obtained assuming a unity Lewis number, thus $D{=}\nu$ and $D_T{=}\nu_T$.

The equation for the variance of the mixture fraction is described by N. Peters[13] and the filtered LES equation for $\widetilde{Z''^2}$ has the following form:

$$\frac{\partial \overline{\rho}\widetilde{Z''^2}}{\partial t} + \frac{\partial}{\partial x_i}\left(\overline{\rho}\widetilde{u_i}\widetilde{Z''^2}\right) = \frac{\partial}{\partial x_i}\left(D_T\overline{\rho}\frac{\partial \widetilde{Z''^2}}{\partial x_i}\right) + 2\overline{\rho}D_T\left(\nabla \widetilde{Z}\right)^2 - \overline{\rho}\widetilde{\chi} \tag{10}$$

In this closure, an eddy turbulent diffusivity closure is employed to close the convective subgrid flux. The closure for filtered scalar dissipation rate ($\widetilde{\chi}$) is an important issue. It represents the effect of subgrid turbulence on $\widetilde{Z}$ which tends to reduce the variance of mixture fraction (since mixing due to the unresolved eddies will tend to reduce the variance of the mixture fraction) and is modeled as $\widetilde{\chi}{=}\ 2D|\ \widetilde{\nabla Z''}\ |^2$.[13] Because $|\ \nabla Z''\ |$ is an unknown quantity, $\widetilde{\chi}$ is computed as $\widetilde{\chi}{=}2\epsilon/k^{sgs}\widetilde{Z''^2}$. The dissipation of the subgrid TKE ϵ in the above expression is directly related to the subgrid kinetic energy: $\epsilon = C_\epsilon(k^{sgs})^{3/2}/\overline{\Delta}$.

3.3 Turbulent Burning Speed

Although the S_L is well defined, in turbulent flow the flame is wrinkled by local fine-scale eddies and this results in an effective increase in burning speed or reactant consumption. Within the context of the thin-flame model, a turbulent flame speed S_T is assumed to exist with which the local flame surface (represented by $\widetilde{G}$) propagates

into the reactant. Thus, $S_F^* = S_T$ in turbulent flow and typically, $S_T = S_T(u', S_L)$. Various models have been proposed but here we employ the Pocheau's model.[15] This model was used in earlier LES studies of gas turbine combustor flows with considerable success.[6,9]

However, additional effect of thermal expansion has to be included. If S_{L_u} is the laminar flame speed with respect to the unburnt gas, the effective laminar flame speed S_L is: $S_L = \rho_u S_{L_u}/\rho$ where ρ_u is the unburnt gas density and ρ is the actual gas density. With this definition, the final form of the turbulent burning speed becomes $S_F^* = S_T(S_L, u^{'})\rho_u/\overline{\rho}$.

3.4 Heat Release

With the flame location and the local flame speed determined, the effect of combustion heat release (and the associated volumetric expansion) on fluid dynamics is included in the LES model. The product temperature T_P is a function of $\widetilde{Z}$ and $\widetilde{Z''^2}$ and is computed during the flamelet library generation. The heat release ΔH is computed as $\Delta H = E_F E(\widetilde{G} - G_0)$. E_F is the heat release corresponding to the entire combustion of the fuel at the specified inflow temperature and pressure and is computed as E_F=$C_P(T_P - T_{COLD})$, where T_{COLD} is the temperature of the unburnt fuel and air mixture and C_P is the specific heat at constant pressure taken as constant. The quantity $(\widetilde{G} - G_0)$ represents the fuel and air mixture state (unburnt, partially burnt or entirely burnt) and E is a filter that can be used to broaden or shrink the thickness of the heat release zone with regard to the thickness of the flame brush. In our study, E = 1.

3.5 LES Prediction of Pollutant Emission

In the present study, we are primarily interested in predicting CO and NO_x emission as a function of the equivalence ratio. The production of these pollutants occurs due to a combined effect of chemical kinetics and turbulent fluid dynamical processes. The local (laminar) kinetic process can be obtained using the flamelet library model but its actual use in the LES filtered equations requires additional considerations which are discussed in the following sections. To track and predict these species mass fraction we solve the following LES filtered species equation:

$$\frac{\partial \overline{\rho}\widetilde{Y}_m}{\partial t} + \frac{\partial}{\partial x_j}\left[\overline{\rho}\widetilde{Y}_m\widetilde{u_j} - \overline{\rho}D_m\frac{\partial \widetilde{Y}_m}{\partial x_j} + \overline{\rho}(\widetilde{Y_m u_j} - \widetilde{Y}_m\widetilde{u_j})\right] = \overline{\rho}\widetilde{\dot{w}}_m \tag{11}$$

Two terms require closure: (i) the subgrid scalar flux $\Phi_{jm}^{sgs} = \overline{\rho}(\widetilde{Y_m u_j} - \widetilde{Y_m}\widetilde{u_j})$ and (ii) the production/destruction term $\overline{\rho}\widetilde{\dot{w}}_m$. In the following, we describe the closures employed for each of these terms for the pollutant species.

The subgrid scalar flux Φ_{jm}^{sgs} is closed using a gradient diffusion closure. This closure is not considered very accurate since the subgrid scalar flux is a small-scale phenomenon and scalar mixing and diffusion occur in the small-scales. However, in a conventional LES, the small-scale mixing is not resolved and therefore, models are needed to close the governing equations. An alternate approach which simulates the scalar fluxes within the subgrid has been developed[10,11] but is not employed here.

In the following sections, we discuss the closure of the chemical source term $\overline{\rho}\widetilde{\dot{w}}_m$ for both CO and NO_x.

3.6 Carbon Monoxide (CO) Closure

CO is formed and/or destroyed by four major mechanisms. All these mechanisms have to be properly modeled in the simulation, and therefore, are discussed in some detail. The four mechanisms (and the nomenclature used to identify them) are:

- Formation of CO at the flame front (subscript ff).
- Oxidation of CO in the post flame region (subscript ox)
- Dissociation of CO_2 (subscript dis)
- Formation of CO formation via oxidation of unburned CH_4 (subscript $oxuhc$)

The overall production/destruction rate of CO can then be written as $\widetilde{\dot{w}}_{CO}=\widetilde{\dot{w}}_{CO,ff}+\widetilde{\dot{w}}_{CO,ox}+\widetilde{\dot{w}}_{CO,dis}+\widetilde{\dot{w}}_{CO,oxuhc}$

In the following, we discuss each of these production/destruction terms.

3.6.1 CO production at the flame front

Due to the presence of radicals in the flame front (especially O), a large amount of CO will be produced via fuel oxidation at the flame front. The flamelet library allows us to determine the fraction of CO formed at the front flame ($Y_{CO,ff}$) as a function of $\widetilde{Z}$ and $\widetilde{Z''^2}$. The formation of CO at the flame front is therefore, treated as a jump relationship, i.e., CO is produced in proportion to the amount of fuel (represented using the $\widetilde{G}$ variable) is consumed.[3,4] Thus, the CO production at the flame front is modeled as:

$$\widetilde{\dot{w}}_{CO,ff} = S_F^* \mid \nabla\widetilde{G} \mid Y_{COff} \tag{12}$$

Typically, CO formation at the flame front ranges, in terms of mass fraction, between 1 and 3 percent.

It should be noted that the value Y_{COff} obtained from the library corresponds to the pollutant formation of a laminar unstretched flame. In the flamelet assumption, the flame is wrinkled by turbulent eddies but cannot change the laminar flame structure. Therefore, turbulence has no direct effect on the CO formation at the flame front, as stated by Eq. (12).

The above assumption is not generally valid since flame stretch can modify the local laminar flame structure (in the thin-reaction zone regime) and this can impact the local CO formation at the flame front. However, at this time, we assume that the entire combustion process occurs in the flamelet regime.

3.6.2 CO oxidation in the post flame region

Once CO is formed, it will be oxidized into CO_2. The flamelet approach allows the determination of the CO oxidation rate as a function of $\widetilde{Z}$ and $\widetilde{Z''^2}$ using the flamelet library. The rate of oxidation of CO is given as $\widetilde{\dot{w}}_{CO,ox} = -\tau_{CO,ox}\widetilde{Y}_{CO}$, where, $\tau_{CO,ox}$ is given by the library. An optimally designed combustion chamber will ensure that the majority of CO formed at the flame front will be oxidized in the post flame region so that the CO mass fraction at the combustion chamber outlet will tend toward the equilibrium value.

The reaction rate of CO oxidation in the post flame region is independent of the subgrid turbulence since the library does not take into account the influence of turbulence. This is a fairly good assumption since the high temperature increases viscous dissipation which in turn, reduces turbulent fluctuations.

3.6.3 CO formation via CO_2 dissociation

The equilibrium value is defined as the CO mass fraction reached when the rate of CO consumption by oxidation equals the rate of CO production via CO_2 dissociation. The mechanism considered here is:

$$CO_2 + H \rightleftharpoons CO + OH \tag{13}$$

The CHEMKIN program allows us to determine the CO mass fraction at equilibrium ($Y_{CO,eq}$). The rate of formation of CO via CO_2 dissociation is taken as:

$$\widetilde{\dot{w}}_{CO,eq} = (1 - \widetilde{G})\tau_{CO,ox} Y_{CO,eq} \tag{14}$$

Note that, when $\widetilde{Y}_{CO} = Y_{CO,eq}$ then $\widetilde{\dot{w}}_{CO,eq} = \widetilde{\dot{w}}_{CO,ox}$, i.e., the rate of oxidation of CO equals the rate of formation of CO via CO_2 dissociation. This approach assumes that the dissociation of CO_2 occurs at an infinitely fast rate. Therefore, Eq. (14) should not be seen as the rate of formation of CO via the dissociation of CO_2 but rather as a correction term allowing $\widetilde{Y}_{CO}$ to tend to $Y_{CO,eq}$.

3.6.4 CO formation via UHC oxidation

CO production also occurs due to the UHC in the flame and post flame zones. UHC production is neglected here because it is assumed that UHC is a negligible source of carbon monoxide. Thus $\widetilde{\dot{w}}_{CO,oxuhc} = 0$.

Once all the terms are combined, the formal LES equation for CO is:

$$\begin{aligned}\frac{\partial \overline{\rho}\widetilde{Y}_{CO}}{\partial t} + \frac{\partial}{\partial x_i}\Big(\overline{\rho}\widetilde{u_i}\widetilde{Y}_{CO}\Big) =& \frac{\partial}{\partial x_i}\Big[(D + D_T)\overline{\rho}\frac{\partial \widetilde{Y}_{CO}}{\partial x_i}\Big] + \\ & \overline{\rho}\Big[S_F^* \mid \nabla \widetilde{G} \mid Y_{CO,ff} - \tau_{CO,ox}\widetilde{Y}_{CO} + (1 - \widetilde{G})\tau_{CO,ox} Y_{CO,eq}\Big]\end{aligned} \tag{15}$$

3.7 Oxides of Nitrogen (NO_x) Closure

Two mechanisms related to NO formation are taken into account in the present study. The first mechanism is the production of NO at the flame front (subscript ff), often called prompt NO, and the second one is the production of NO due to the Zeldovich mechanism in the post flame region (subscript zel), often called thermal NO. Thus, the reaction rate for NO can be written as $\widetilde{\dot{w}}_{NO} = \widetilde{\dot{w}}_{NO,ff} + \widetilde{\dot{w}}_{NO,zel}$

Due to the large amount of O radical in the flame region, NO is formed as the gases pass through the flame front. The amount of NO released at the flame front $Y_{NO,ff}$ and the production rate $\widetilde{\dot{w}}_{NO,ff}$ are computed via the flamelet library as a function of $\widetilde{Z}$ and $\widetilde{Z''^2}$. The rate of formation ($\widetilde{\dot{w}}_{NO,ff}$) is computed with the same method used for the rate of formation of CO. Thus,

$$\widetilde{\dot{w}}_{NO,ff} = S_F^* \mid \nabla \widetilde{G} \mid Y_{NO,ff} \tag{16}$$

The rate of formation of NO in the post flame region is computed using the Zeldovich mechanism under the quasi-steady assumption, i.e., the concentration of O and N radicals are assumed equal to the O and N concentrations at equilibrium. The Zeldovich mechanism considered herein is:

$$\begin{aligned} N_2 + O &\rightleftharpoons NO + N \\ O_2 + N &\rightleftharpoons NO + O \end{aligned} \tag{17}$$

Under the quasi-steady assumption, where O, N, N_2 and O_2 mass fraction are considered to be constant, the rate $\dot{w}_{NO,zel}$ is computed as a function of $\widetilde{Z}$ and $\widetilde{Z''^2}$. Thus, the reaction rate for NO formed via the Zeldovich mechanism ($\widetilde{\dot{w}}_{NO,zel}$) in the post flame region is:

$$\widetilde{\dot{w}}_{NO,zel} = \big(1 - \widetilde{G}\big)\dot{w}_{NO,zel} \tag{18}$$

Nevertheless, the reaction:

$$N_2 + O_2 \rightleftharpoons 2NO \tag{19}$$

is considered to be far from equilibrium. Therefore, the rate of formation $\dot{w}_{NO,zel}$ of NO in the post flame region is constant and independent upon the NO mass fraction.

The final LES NO governing equation is:

$$\begin{aligned} \frac{\partial \overline{\rho}\widetilde{Y}_{NO}}{\partial t} + \frac{\partial}{\partial x_i}\Big(\overline{\rho}\widetilde{u}_i\widetilde{Y}_{NO}\Big) =& \frac{\partial}{\partial x_i}\Big((D + D_T)\overline{\rho}\frac{\partial \widetilde{Y}_{NO}}{\partial x_i}\Big) + \\ & \overline{\rho}\Big(S_F \mid \nabla \widetilde{G} \mid Y_{NO,ff} + \big(1 - \widetilde{G}\big)\dot{w}_{NO,zel}\Big) \end{aligned} \tag{20}$$

4 Numerical Approach

The LES equations described above are solved using a finite-volume scheme that is nominally second-order accurate in both space and time. Details of the combustor geometry and the numerical approaches are summarized below.

4.1 The DOE-HAT Geometry

The geometry of the DOE-HAT combustor is shown in Fig. 1. In this combustor, the premixed methane-air mixture enters the combustor in a swirling manner through an annular slot. The flame is stabilized by the recirculation in the base of the dump and also by the recirculation created by the center body. Fig. 2 shows the characteristic grid distribution.

The length of the combustion chamber is 0.6 m, its radius is 0.053 m and the inlet is located between 0.0173 m and 0.0314 m measured from the centerline. The length of the combustor is chosen so that the emissions predictions (which are only available at 0.381 m from the dump plane) can be computed and compared with data.

The inflow characteristics are chosen as given in the earlier DOE-HAT experiment: the fuel is methane (CH_4) and the reactants enter the combustor with a temperature of 700 K, a pressure of 1.378 MPa., and a mean inflow velocity of 68.6 m/s. The swirl in the flow is characterized by a swirl number of 0.6, the swirl number being defined in[6]

and the reference radius used is the outer diameter of the inflow pipe. Inflow velocity profiles are obtained from experimental results. The Reynolds number based on the inlet velocity and the diameter of the center-body is 120,000. A random turbulent field is added to the inflow mean velocity and a subgrid turbulence intensity of 7 percent is used to specify the incoming subgrid kinetic energy. Characteristic based inflow and outflow boundary conditions[16] are employed for all the reported simulations.

4.2 3D Grid Topology

In order to resolve the shear layer and the flame features without the centerline restrictions when a cylindrical grid is used, a two-grid approach is used in this study. The region near the centerline is resolved using a rectangular grid and a cylindrical grid is used for the rest of the domain. Second-order interpolation between the two grid is employed to transfer information back and forth. This two-grid approach is shown in Fig. 2. For the current combustor, all the combustion processes occur in regions far from the centerline and the two-grid approach effectively eliminates the centerline time step restriction without impacting the physics of interest. Studies were conducted by varying the grid resolution and the size of the inner grid to ensure smooth continuity between the solutions in each of the two grids, and also to ensure grid independence is achieved for the resolved scales. The grid resolution used for all the studies reported here is 200x81x101 for the cylindrical grid and 200x22x22 for the inner Cartesian grid. The grid is clustered in the region of high shear to resolve the flame zone.

This numerical algorithm is implemented in parallel using Message-Passing Interface (MPI). The two grids overlap, and so, once the MPI operations are completed, the interpolation depends only on the information contained in one grid. In the present application, only a 2D interpolation at each axial location is carried out and seems to suffice. A quantity f at a location (y,z) is determined using the information from the closest computed points. The interpolation method used here is described elsewhere.[17]

To ensure $O(2)$ accuracy in the interpolation, both the centerline Cartesian and the cylindrical grid are uniform in the vicinity of the centerline. The inaccuracy in the interpolation caused by the curvature of the cylindrical grid is neglected at present, and this issue will be revisited later.

Our studies suggest that, to avoid numerical oscillations at the interface between the two grids, the boundary between two grids should not lie in region of high shear or in regions of high pressure or density spatial gradients.

Computations were carried out entirely in parallel using MPI libraries. The LES solver is highly optimized for scalability on nearly all parallel machines, and achieves a speed of $2.4\text{x}10^{-5}$ CPU seconds per time step, per grid point, per processor, on Compaq SC40 machine. Multiple flow through times (typically 3-4) are recorded (after the initial transients) to obtain stationary statistics. Typically, for the grid noted above approximately 896 single-processor hours are needed for a single flow through time realization. Thus, a complete simulation with reliable statistics will require around 2700 single processor hours. Using 56 processors, this reduces to 50 wall clock hours.

5 Results and Discussion

To study combustion dynamic and pollutant production as LBO is approached, a range of equivalence ratio from 0.41 to 0.53 conditions is studied. Experiments[1] have

shown that the lowest value (Φ=0.41) is close to LBO. Representative results for these simulations are discussed in the following sections.

5.1 Flame Characteristics

Change in the equivalence ratio directly influences the propagation speed and therefore, impact the flame shape (length) and the sensitivity of the flame to turbulent motion. As the equivalence ratio decreases, the laminar flame speed decreases and thus, the flame length increases. This has a direct influence upon the pollutants formation at the flame front.

Furthermore, as the laminar flame speed decreases, the flame surface becomes more sensitive to the turbulent motion, or, in other words, the interactions between the flow and the flame increases. This is shown in Figs. 3 and 4. For Φ=0.53 (Fig. 3) the flame surface is wrinkled primarily by the large vortical structures created at the edge of the inflow pipe whereas for Φ=0.41, the flame shape is also affected by the smaller turbulent structures (Fig. 4). Since the turbulent flame speed is a function of u'/S_L, small changes in u' have a great impact on the flame propagation speed for a fixed S_L and this influence increases as Φ decreases (because S_L decreases). The impact of this dynamics on pollutant emission fluctuation is discussed in the following section.

5.2 CO emission

The physics that impact CO emission is investigated in detail by addressing the contribution of the aforementioned three mechanisms of CO production. (Note that the fourth mechanism, CO formation via UHC, is neglected in the present study.)

5.2.1 Source(s) of CO production

Since CO emission in the combustor is due to a combination of different processes, not occurring at the same location, it is necessary to investigate the relative contribution of these mechanisms to the overall CO emission. This comparison is shown in Fig. 5. It can be seen that the CO emission due to CO_2 dissociation is decreasing with the equivalence ratio. This is due to the fact that, as the equivalence ratio decreases, the temperature of the burnt product decreases and thus, the equilibrium of the reaction mechanism (described by Eq. (13)) shifts to the left.

On the other hand, the CO emission when the CO_2 dissociation is not taken into account increases as the equivalence ratio decreases. This is the combined effect of two mechanisms: CO production across the flame and CO oxidation in the post flame region. These results suggest a question: is the increase in CO emission with decreasing Φ due to increased CO formation at the flame front or due to a lower oxidation rate? In Fig. 6, the average CO mass fraction is plotted against the axial distance from the dump plane for different Φ. The initial increase in CO mass fraction is due to the CO formation at the flame front. However, beyond the flame, CO mass fraction decreases due to CO oxidation. This mass fraction decreases till equilibrium of Eq. (13) is reached. Furthermore, at lower equivalence ratio, the product temperature is lower and thus, the CO oxidation rate is also lower.

Figure 5 also shows that CO production at the flame increases with decreasing Φ. Since CO formation per unit area at the flame front decreases as the equivalence ratio decreases, the observed increase in CO at the flame front is explained by an increase in

the flame area. The flame surface area increases as Φ is reduced since u'/S_L increases with decrease in S_L.

5.2.2 Comparison with experiments

Numerical results are compared with experimental data in Fig. 7. Very good agreement is observed at all simulated conditions. CO emission shows a minima as a function of equivalence ratio in excellent agreement with data. A critical equivalence ratio is defined Φ_{CR} (in the present case, $\Phi_{CR} = 0.44$) for which CO emission is at a minimum. When $\Phi > \Phi_{CR}$, the total amount of CO produced at the flame front will be oxidized before reaching the emission probe. Thus, the measured emission will be determined by the equilibrium between CO_2 dissociation and CO oxidation. The mass fraction of CO at equilibrium computed using CHEMKIN is thus, a good approximation up to some values of $\Phi > \Phi_{CR}$. This is shown in Fig. 8 where the CO at equilibrium and the experimental emission data are plotted. For $\Phi > \Phi_{CR}$, the CO mass fraction computed by CHEMKIN agrees very well with measurements within the range of current interest. Note that an over-prediction occurs at higher values of Φ which suggests that equilibrium CO production is not sufficient to explain CO emission at high Φ. This is an issue that will be addressed in the future.

When $\Phi < \Phi_{CR}$, the amount of CO at equilibrium is negligible and thus, CO emission is determined by the balance between CO production at the flame front and CO oxidation in the post flame region. With decrease in Φ there is more production at the flame front and less oxidation due to lower flame temperature. Therefore, CO mass fraction measured at the emission probe increases when the equivalence ratio decreases. This phenomena has been called kinetic CO by Lefebvre.[18]

5.2.3 Fluctuation in CO emission near LBO

Figure 9 shows the normalized RMS fluctuation of the CO mass fraction ($Y_{CO,RMS}/\overline{Y_{CO}}$). Only the region located two flame length downstream the dump plane is shown. In general, the fluctuations decrease with axial distance due to turbulent mixing and also due to the "damping" effect of CO consumption via oxidation. The fluctuations tends to zero as Eq. (13) tends toward equilibrium. These results are summarized later in Table 1. When, at the location of the emission probe, Eq. (13) is at equilibrium (for Φ=0.53 and Φ=0.45) the RMS of the CO mass fraction fluctuations are negligible. But, for Φ=0.41 CO does not reach its equilibrium value at the location of the emission probe and the fluctuation level is nearly 21 percent. This figure exhibits an interesting trend. The fluctuations are intense closer to the dump plane for high Φ but the magnitude decreases and the location moves further downstream as the equivalence ratio is decreased. On the other hand, the decay in RMS fluctuation with axial distance is larger at high Φ. For Φ=0.44 the decrease is RMS is more gradual such that at the location of the emission probe the lowest Φ shows the largest RMS value.

These results appear to contradict the earlier observation that as the equivalence ratio is reduced local flame fluctuations increase due to the reduced stability of the flame and therefore, fluctuations in the CO should also increase. But, as shown in Fig. 9, closer to the dump plane CO fluctuation increases with increase in Φ. This apparent disagreement can be explained by investigating the interaction between the vortical flow at the dump plane and the flame.

Previous work[19] has shown that strong interactions between large scale coherent structures and flame surface exist for a swirl number above a critical value. The

present simulations suggest that similar interactions are also present in the DOE-HAT combustor 3. This is confirmed by Figs. 10 and 11 where the frequency spectra of the azimuthal vorticity (w_Θ) in the vicinity of the dump plane (this being an indicator of the behavior of the coherent structures described above) and the frequency spectra of the CO mass fraction fluctuation are plotted versus the Strouhal number (St). St is defined as $St = fD_0/U_0$ where D_0 is the diameter of the inlet pipe and U_0 is the inflow bulk velocity. For both Φ, the frequency of w_Θ and Y_{CO} peak at the same St, indicating that coherent structures influence the flame surface area that, in turn, influences the amount of CO produced at the flame surface. Comparison of Figs. 3 and 4 show that, for Φ=0.53, the flame surface is strongly perturbed by the coherent structures, whereas, these perturbations are considerably smaller for Φ=0.41. Thus, CO fluctuations are lower near the dump plane for Φ=0.41 when compared to Φ=0.53 case. Further downstream, the fluctuations rapidly decrease for the high Φ cases, whereas, for the low equivalence ratio case, the intensity is still significant. This is a direct result of the "damping" effect of the CO oxidation that decreases with the equivalence ratio. Thus, at the emission probe location, the low Φ case exhibits a higher RMS of the CO mass fraction.

The frequency of the CO mass fraction oscillations is also affected by changes in Φ. The peak frequency in CO (as well as in vorticity) is St=1.57 for Φ=0.41 and St=2.67 for Φ=0.53. These values of Strouhal number are in the range of values for the jet preferred mode seen in both non-reacting[20] and reacting flows.[21] However, due to the annular nature of the DOE-HAT combustor, some deviation is naturally expected. It is also expected that the magnitude of the heat release (and the connected volumetric expansion) can change the frequency of the jet preferred mode since it can impact the structure and propagation characteristics of vortices.[22] This is observed here as well.

5.2.4 UHC influence upon CO emission

As noted earlier in Section 3.6.2, the unburnt CH_4 released when the flame is quenched due to aerodynamic stretch is not considered in this study. This unburnt CH_4 or UHC can be an important source of CO in the post flame region since (due to the high temperature of the post flame region) UHC will not reignite but will be oxidized and form CO. Aerodynamic quenching can be important for low equivalence ratio and can thus, influence the CO emissions. Earlier studies by Held *et al*[4] in a GEAEC LM-6000 combustor showed that post-flame UHC oxidation provides a significant source of CO late in the combustion process. For the present DOE-HAT combustor, however, the good agreement between our LES prediction and experimental data suggests that this mechanism is not that significant, at least at the measurement location. Nevertheless, the UHC effect on CO emission in this combustor remains an issue to be resolved.

5.3 NO Emission

Both thermal and prompt NO emission are modeled in this study and the results are summarized below.

5.3.1 Comparison with experiments

Figure 12 shows that the NO emission trend is well predicted by the LES simulations. However additional NO is also produced via the Zeldovitch mechanism in the post flame region. The combination of emission at the flame front and in the post flame region

(which includes the recirculation zone at the base of the dump plane) determines the total NO_x production. The under-prediction at high Φ is explained below by analyzing the source of prompt and thermal NO in the combustor.

To evaluate the relative importance of both these mechanisms, NO mass fraction as a function of the axial distance is shown in Fig. 13. For Φ=0.41 and Φ=0.45 the initial increase in NO mass fraction is due to the NO formation at the flame front while formation in the post-flame region is negligible. For these equivalence ratios, the major NO formed at the flame front is due to the relatively low temperature in the post flame region, and no significant amount of NO is produced via the Zeldovitch mechanism. However, for $\Phi = 0.53$ the temperature of the burnt gases is higher and thus, the NO production via the Zeldovitch mechanism becomes significant. As a result, NO mass fraction increases in the post-flame region. This observation is in agreement earlier studies[23] of a lean premixed-prevaporized (LPP) combustor where it was prove that NO does not increase significantly with distance downstream of the combustion zone for equivalence ratio lower than 0.5 and that, above this value, the formation of NO in the post flame region becomes an important mechanism.

For Φ=0.53, the NO mass fraction initially decreases and then increases, with a minimum around 70 mm from the dump plane. In the far field, NO level increases linearly because Eq. (19) is far from equilibrium and the rate of formation of NO in the post-flame region is constant. The increase is due to the post flame thermal NO production via the Zeldovitch mechanism. These results provide an explanation for the observed differences between the predicted and measured NO emission, and of the fact that this difference increases with an increase in Φ. The influence of the Zeldovitch mechanism being negligible for $\Phi < 0.5$, and therefore, the under-prediction is directly related to the under-prediction of NO formation at the flame front. The NO formation at the flame front is related to the flame surface and mass fraction of NO formed by a flame element. The fact that CO predictions are in good agreement with the experimental results suggests that the flame surface (and its area) is probably well predicted. Thus, the under-prediction of NO formation at the flame front can only be explained by an under-prediction of $Y_{NO,ff}$ by the library. One the other hand, since the amount of NO produced via the Zeldovitch mechanism is directly proportional to the amount of NO formed at the flame front (the rate of formation via the thermal mechanism is $\dot{w}_{NO,EQ_{CHEMKIN}}\widetilde{Y_{NO}}$), the difference between the predicted and measured NO is also expected to increase as the influence of the Zeldovitch mechanism increases, i.e., as the equivalence ratio increases.

Additional possibilities could also exist since, in this study, neither the extended Zeldovitch mechanism nor the N_2O-intermediate route were considered.[24] These issues will be addressed in a future study.

5.3.2 Fluctuation in NO emission near HBO

The normalized RMS of the NO mixture fraction is plotted against the distance from the dump plane in Fig. 14. The mixing region from the dump plane and extending approximately twice the flame length is not plotted in this figure. The RMS of the fluctuation decreases with distance from the dump plane for all Φ's. For low equivalence ratios (Φ<0.5), the thermal NO mechanism is negligible, and mixing and diffusion processes damp the oscillations (similar to their effect on CO). For higher equivalence ratios (Φ>0.5), the additional NO formation in the post-flame region tends to increase the oscillations.

5.4 Summary of CO and NO emission

Finally, to summarize the above discussion, emissions prediction from the numerical and experimental study are recapitulated in Table 1.

6 Conclusion

In this study, a LES methodology that combines a thin-flame model for flame tracking, along with transport models for CO and NO species is used to predict emission and unsteady dynamics in a full-scale DOE-HAT combustor under experimental conditions. Subgrid closures for the LES model are developed and implemented for this study. The effect of varying the equivalence ratio is studied and the results are compared with experimental data for CO and NO emission.

The simulations show that an increase in flame oscillation (and associated flow oscillation) occurs as the LBO limit is approached. These results are consistent with experimental observations.

Very good agreement with measurements are obtained for both CO and NO over a significant range of equivalence ratios. This study also allowed a better understanding of the various mechanisms leading to an exponential increase in the CO emission as the lean flammability limit is reached. The dominant mechanism when the equivalence ratio is large is the CO equilibrium process, but when the equivalence ratio is close to the lean flammability limit, the mechanism controlling the CO emission is the CO production at the flame front. Furthermore, link between flame, vortex shedding and emission dynamic is investigated and discussed.

The prediction of NO emissions is also reasonable. The contribution of both prompt and thermal mechanisms is evaluated, and the analysis suggests that post flame production is only significant for high equivalence ratio. This result is also in good agreement with past observations in LPP gas turbines systems.

7 Future Plans.

If emission as LBO limit is approached was predicted, the current implementation is not able to capture the processes occurring in the LBO domain. The G-equation approach is incapable of capturing the actual LBO since flame extinction (both local and global) and re-ignition can not be modeled using this approach. Therefore a new approach based on the Linear Eddy Model (LEM) subgrid closure with multi-steps kinetics is being used to revisit this problem. In the subgrid LEM approach, scalar reaction-diffusion processes are simulated within the subgrid (i.e. within each LES cell) using a localized 1D stochastic model that mimics the influence of turbulence at the subgrid level. This implies that the LEM methodology is able to capture the effect of small scales fluctuations.

In order to be able to predict flame quenching, which principle cause will be high aerodynamic stretch, a 5 reactions - 9 species mechanism has to be used. Since the computational cost of such a chemistry could be considerable, an In-Situ Adaptive Tabulation (ISAT) approach will be applied in order to speed up the chemistry calculation.

The next effort will be realized in two phases. The first phase is to use a relatively computationally cheap 1-step 5 species global chemistry. While the flame will be re-

solved at the LEM level, emission will be tracked at the LES level using the flamelet library approach. The goal of this study is to reproduce the previously obtained emission prediction with a method that predict the flame structure and behavior more precisely than the G-equation approach. The second phase is to implement the 5-steps, 9 species chemistry. In this last methods, NO and CO are directly taken into account in the chemical mechanism. Thus the flamelet library will not be used. The other main advantage of this chemistry mechanism is its ability to predict flame quenching and re-ignition. Thus, this method will accurately describes the flame structure and dynamics as well and the emission characteristics.

The first phase of the previously described schedule is underway.

8 Acknowledgments

This work was made possible with the support in part by the Department of Energy and CFD Research Corporation, AL. Support for the flamelet library was provided by General Electric Aircraft Engine Company. Support for the computations was provided by DOD HPC Center at ERDC (MS).

References

[1] A. Bhargava, D. W. Kendrick, M. B. Colket, W. A. Sowa, K. H. Casleton, and D. J. Maloney. Pressure effects on nox and co emission in industrial gas turbines. *Trans. of the ASME*, 2000-GT-8, 2000.

[2] T. J. Held and H. C. Mongia. Application of a partially premixed laminar flamelet model to a low-emission gas turbine combustor. *ASME-98-GT-217*, 1998.

[3] T. J. Held and H. C. Mongia. Emissions modeling of gas turbine combustors using a partially-premixed laminar flamelet model. *AIAA-98-3950*, 1998.

[4] T. J. Held, M. A. Mueller, and H. C. Mongia. A data-driven model for no_x, co and uhc emissions for a dry low emissions gas turbine combustor. *AIAA-2001-3425*, 2001.

[5] G. Erlebacher, M. Y. Hussaini, C. G. Speziale, and T. A. Zang. Toward the large-eddy simulation of compressible turbulent flows. *Journal of Fluid Mechanics*, 238:155–185, 1992.

[6] W.-W. Kim, S. Menon, and H. C. Mongia. Large-eddy simulation of a gas turbine combustor flow. *Combustion Science and Technology*, 143:25–62, 1999.

[7] C. C. Nelson and S. Menon. Unsteady simulations of compressible spatial mixing layers. *AIAA-98-0786*, 1998.

[8] W.-W. Kim and S. Menon. A new incompressible solver for large-eddy simulations. *International Journal of Numerical Fluid Mechanics*, 31:983–1017, 1999.

[9] W.-W. Kim and S. Menon. Numerical simulations of turbulent premixed flames in the thin-reaction-zones regime. *Combustion Science and Technology*, 160:119–150, 2000.

[10] V.K. Chakravarthy and S. Menon. Large-eddy simulations of turbulent premixed flames in the flamelet regime. *Combustion Science and Technology*, 162:1–48, 2000.

[11] V.K. Chakravarthy and S. Menon. Subgrid modeling of premixed flames in the flamelet regime. *Flow, Turbulance and Combustion*, 2001.

[12] J. R. Kee, F. M. Rupley, and J. A. Miller. Chemkin-ii a fortran chemical kinetics package for the analysis of gas phase chemical kinetics. Technical Report SAND89-8009B, Sandia National Laboratories, 1992.

[13] N. Peters. *Turbulent Combustion.* Cambridge Monographs on Mechanics, 2000.

[14] A. R. Kerstein, Wm. T. Ashurst, and F. A. Williams. The field equation for interface propagation in an unsteady homogeneous flow field. *Physical Review A*, 37:2728–2731, 1988.

[15] A. Pocheau. Scale invariance in turbulent flont propagation. *Physical Review E*, 49:1109–1122, 1994.

[16] T. Poinsot, D. Veynante, and S. Candel. Quenching processes and premixed turbulent combustion diagrams. *Journal of Fluid Mechanics*, 228:561–606, 1991.

[17] S. C. Chapra and R.P Canale. In *Numerical methods for enginneers.* McGraw Hill International, 1990.

[18] A. H. Lefebvre. *Gas Turbine Combustion.* Taylor and Francis, second edition, 1999.

[19] C. Stone and S. Menon. Dynamics and analysis of vortex-flame interaction in swirling combustion flows. In *Proceedings of second International Symposium on Turbulent and Shear Flow Phenomena*, pages 485–490. Begel House, 2001.

[20] T. P. Gutmark and C. M. Ho. On the preferred modes and the spreading rates of jets. *Journal of Fluid Mechanics*, 26:2932–2938, 1983.

[21] Parr D. M. Gutmark, T. P. and K. C. Schadow. Three-dimensional structures of an axisymmetric reacting jet. *AIAA 87-0148, 26th AIAA Aerospace Sciences Meeting*, 1987.

[22] C. Stone and S. Menon. Numerical simulation of combustion dynamics in a swirling dump combustor. In *Proceedings of Grand Challenges In Computer Simulations, High Performance Computing 2001*, pages 15–20. SCS Press, 2001.

[23] G. Leonard and S. Correa. Nox formation in premixed high pressure lean methane flames. *Fossil Fuel Combustion Symposium*, pages 69–74, 1990.

[24] S. R. Turns. *An Introduction to Combustion. Concept and Applications.* Mac Graw Hill, 1999.

Location (mm)	Equivalence ratio	CO LES	CO Experiments	CO_{RMS} (percent)	NO LES	NO_{RMS} (percent)	NO Experiments
100	0.53	11.4	NO DATA	3.0	3.8	3.0	NO DATA
	0.45	858.0		44.3	1.12	1.56	
	0.41	2985.0		NO DATA	0.52	NO DATA	
200	0.53	10.6	NO DATA	0.05	4.4	1.6	NO DATA
	0.45	34.8		33.6	1.13	0.45	
	0.41	677.0		22.7	0.53	0.78	
300	0.53	10.6	NO DATA	0.02	5.0	1.2	NO DATA
	0.45	2.3		8.3	1.14	0.40	
	0.41	116.0		18.9	0.55	0.46	
381	0.53	10.6	9.5	0.00	5.40	1.30	8.3
	0.45	1.7	1.6	0.05	1.15	0.50	2.4
	0.41	25.6	32.8	17.5	0.56	0.43	0.9

Table 1: Predicted mean CO and NO emissions (in ppm with 15 percent excess O_2) and the normalized RMS ($Y_{RMS}/\overline{Y}$) of their fluctuations (in percentage). Data reported at the location of the experimental emission probe.

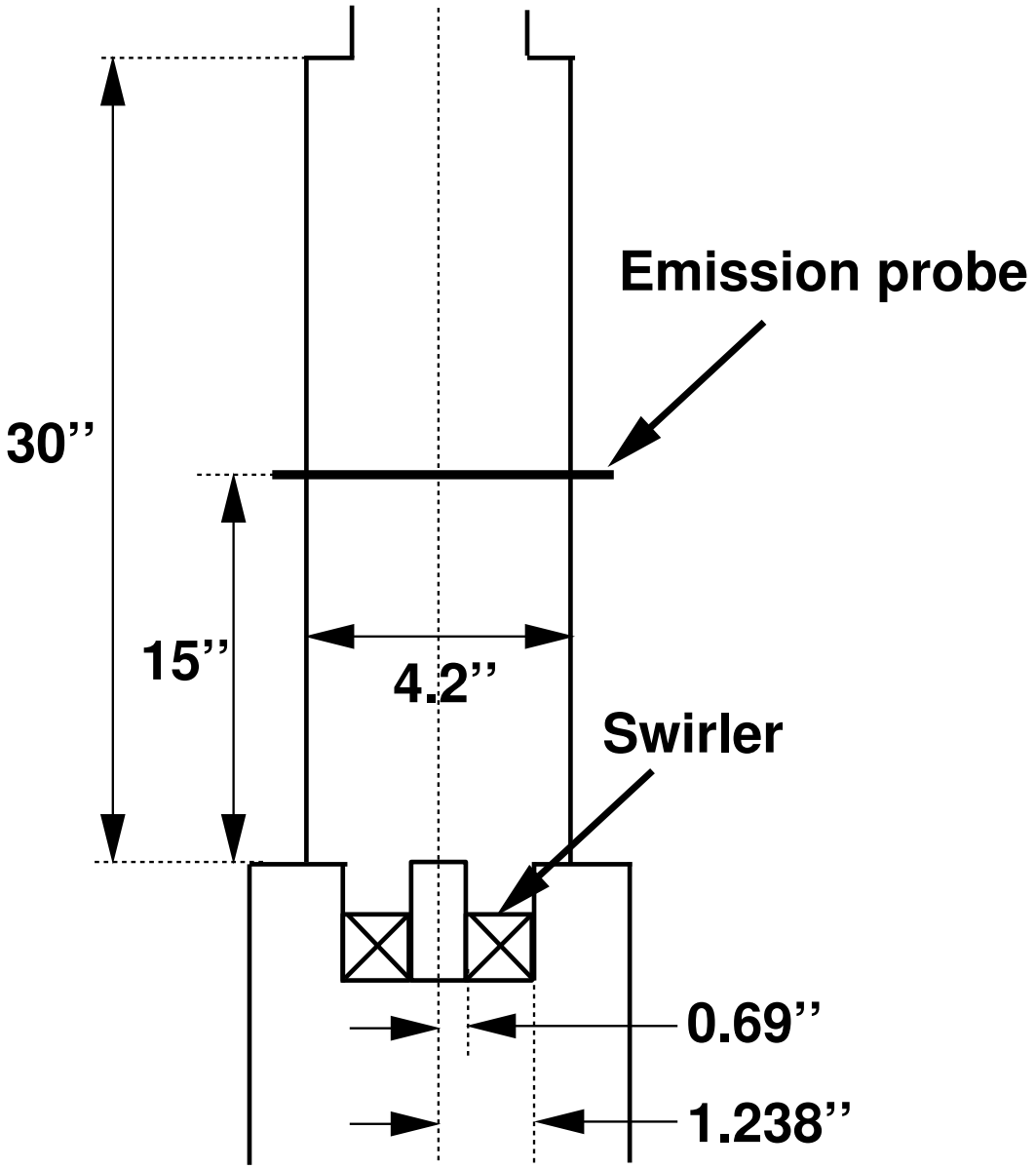

Figure 1: Sketch of the DOE-HAT Combustor setup. All dimensions are given in inches.

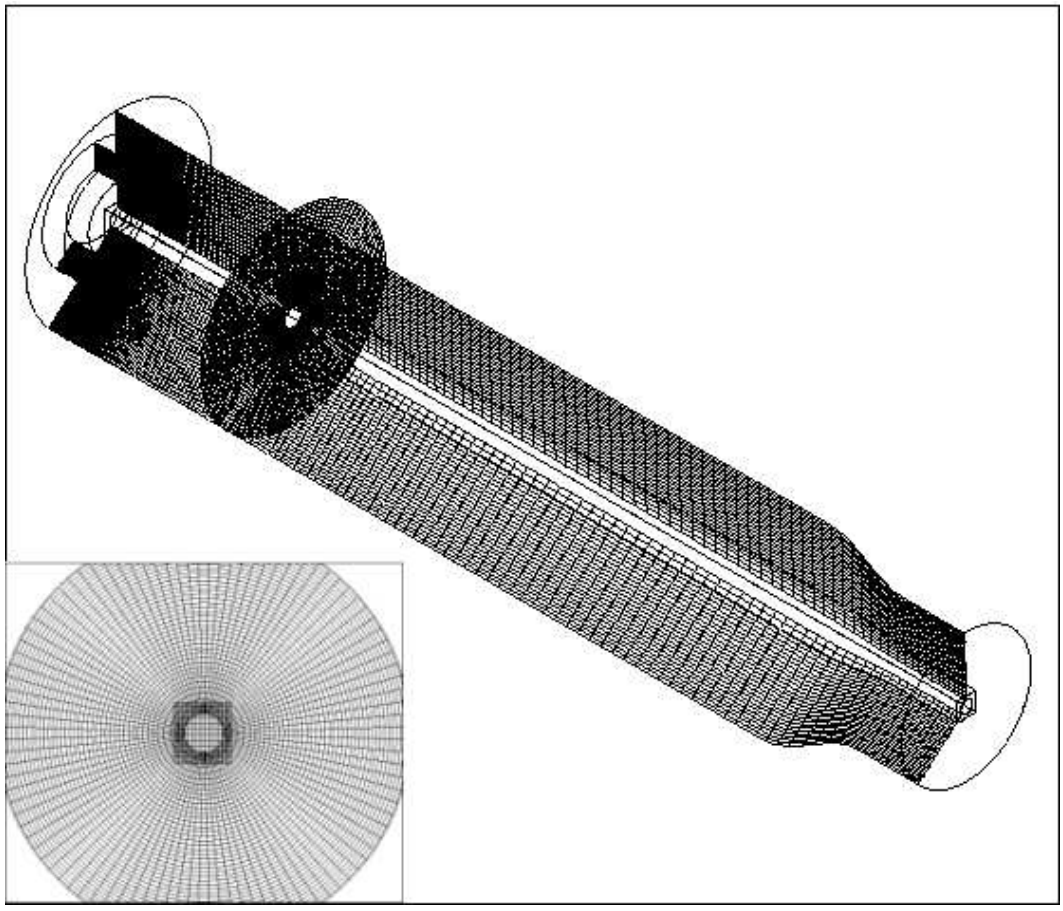

Figure 2: General perspective view of the 3D computational domain and grid. Front view of the grid mesh showing the cartesian grid (inside) and the cylindrical grid (outside).

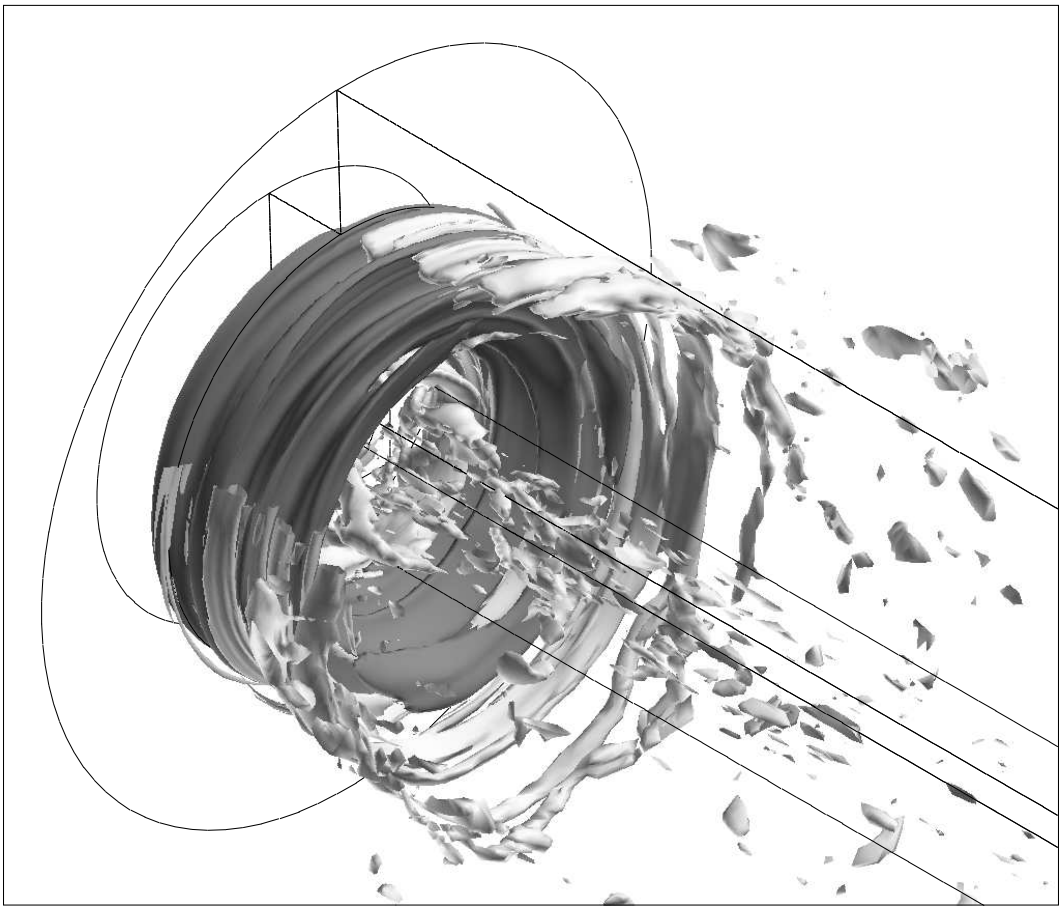

Figure 3: Flame surface for $\Phi = 0.53$ (dark) and azimuthal vorticity isosurface (light) - w_θ = 15,000 s^{-1}

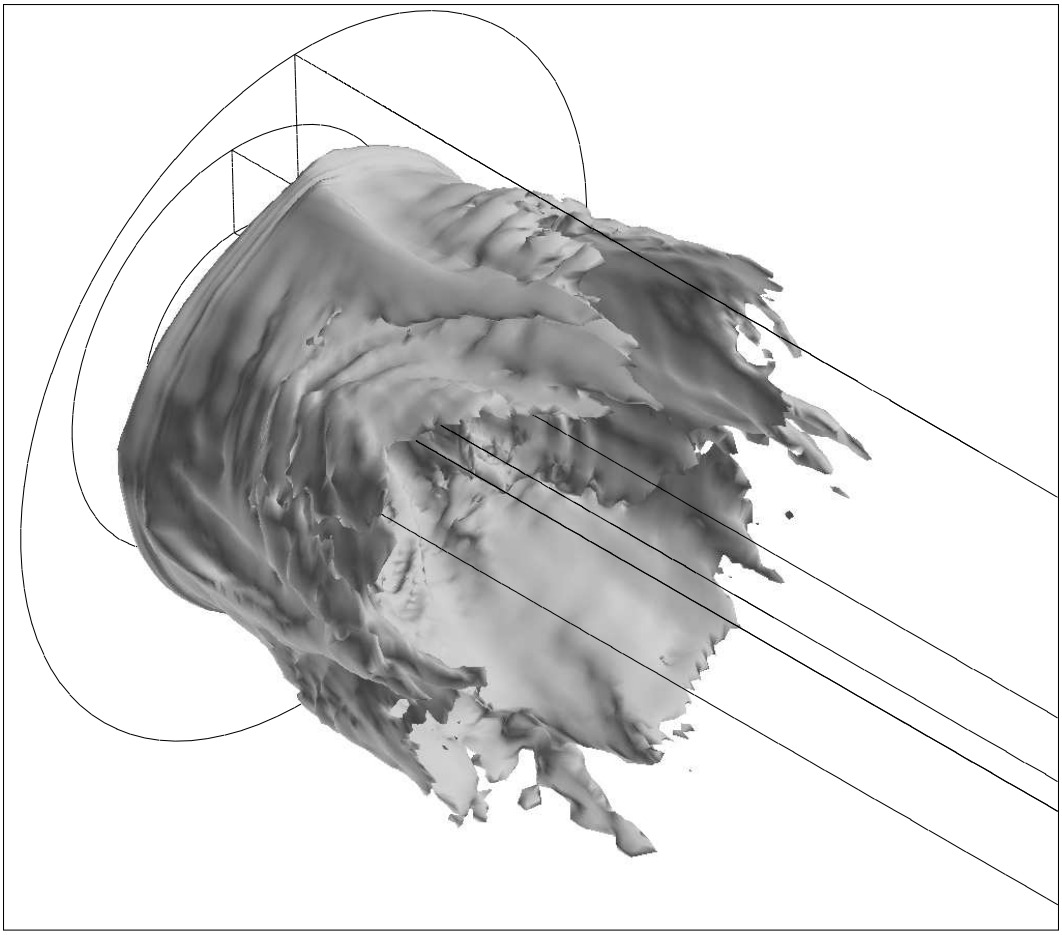

Figure 4: Flame surface for $\Phi = 0.41$

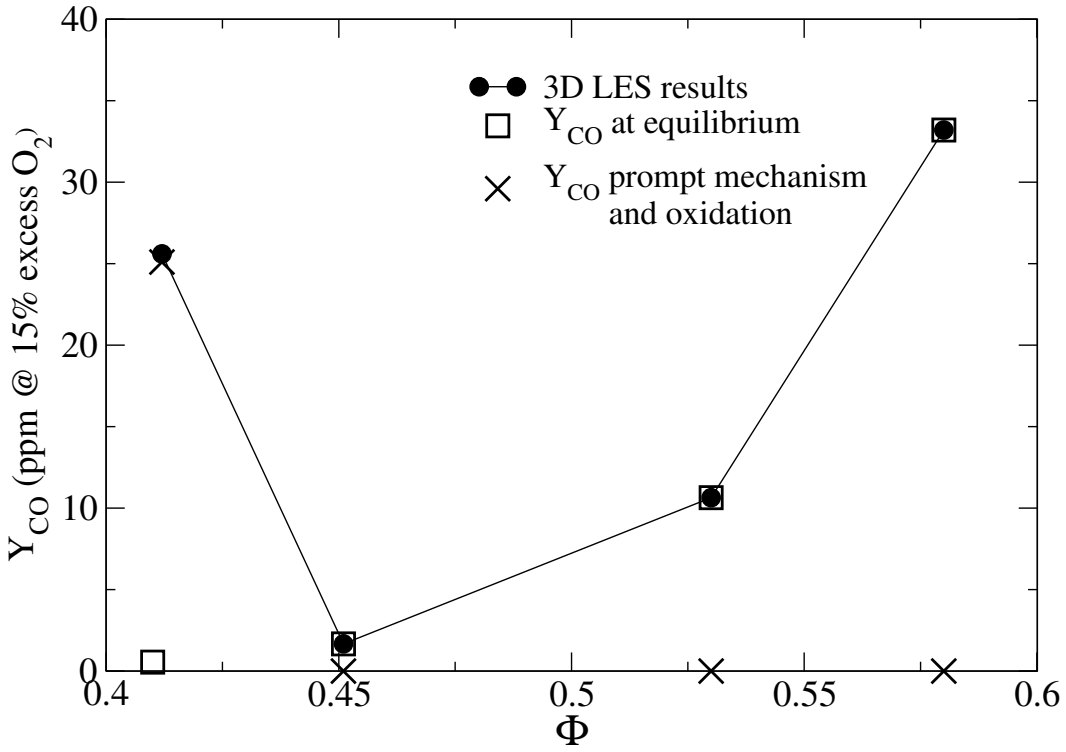

Figure 5: Influence of different CO mechanisms on the overall CO emission. The numerical results, CO mass fraction at equilibrium and CO mass fraction due to prompt mechanism and oxidation mechanisms are plotted. Results are shown at the location of the emission probe

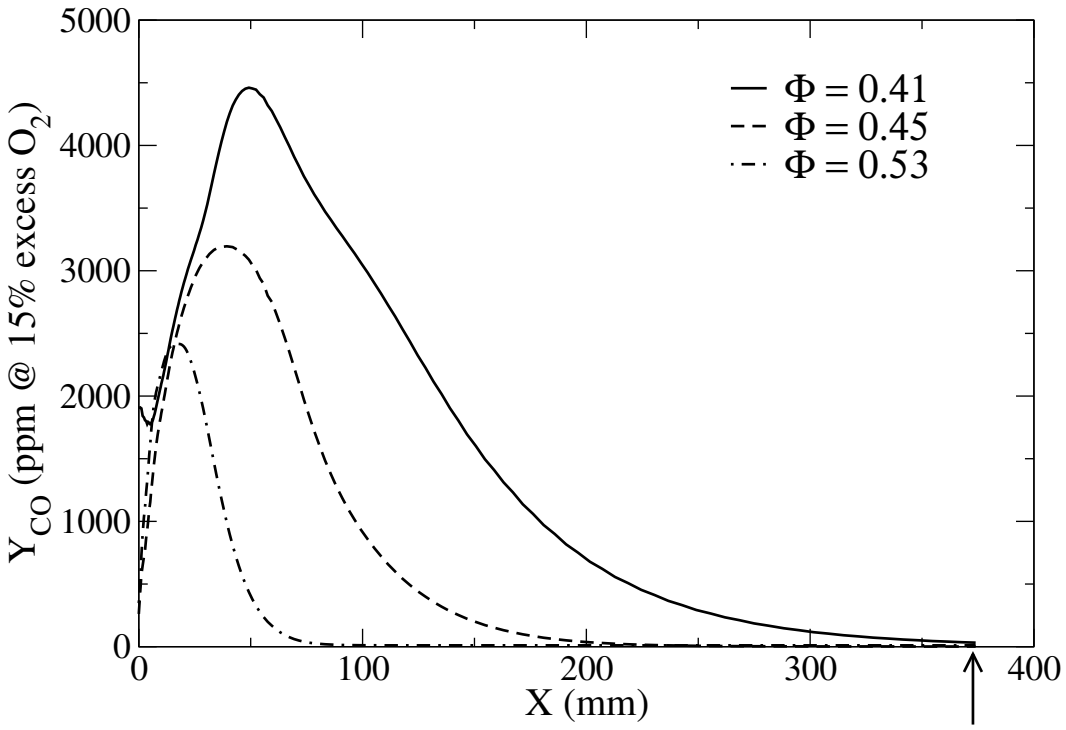

Figure 6: CO mass fraction (in ppm @ 15 percent excess O_2) as a function of axial distance from the dump plane for different equivalence ratio. The location of the emission probe is shown by an arrow.

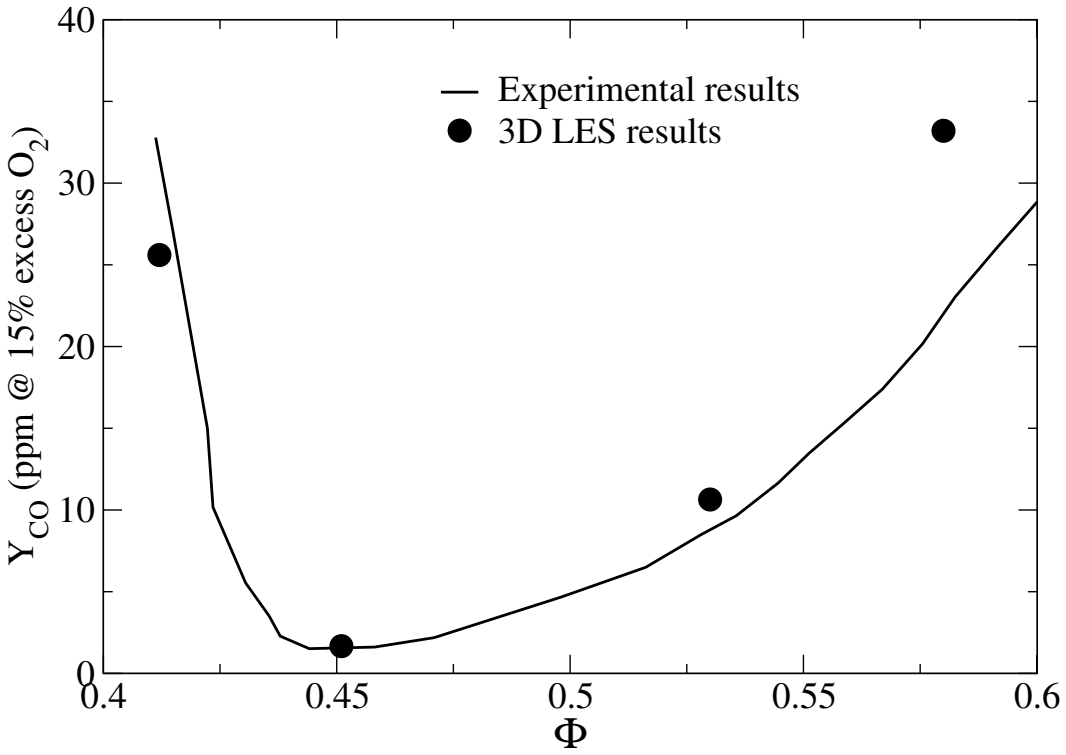

Figure 7: CO mass fraction (in ppm @ 15 percent excess O_2) as a function of the equivalence ratio.

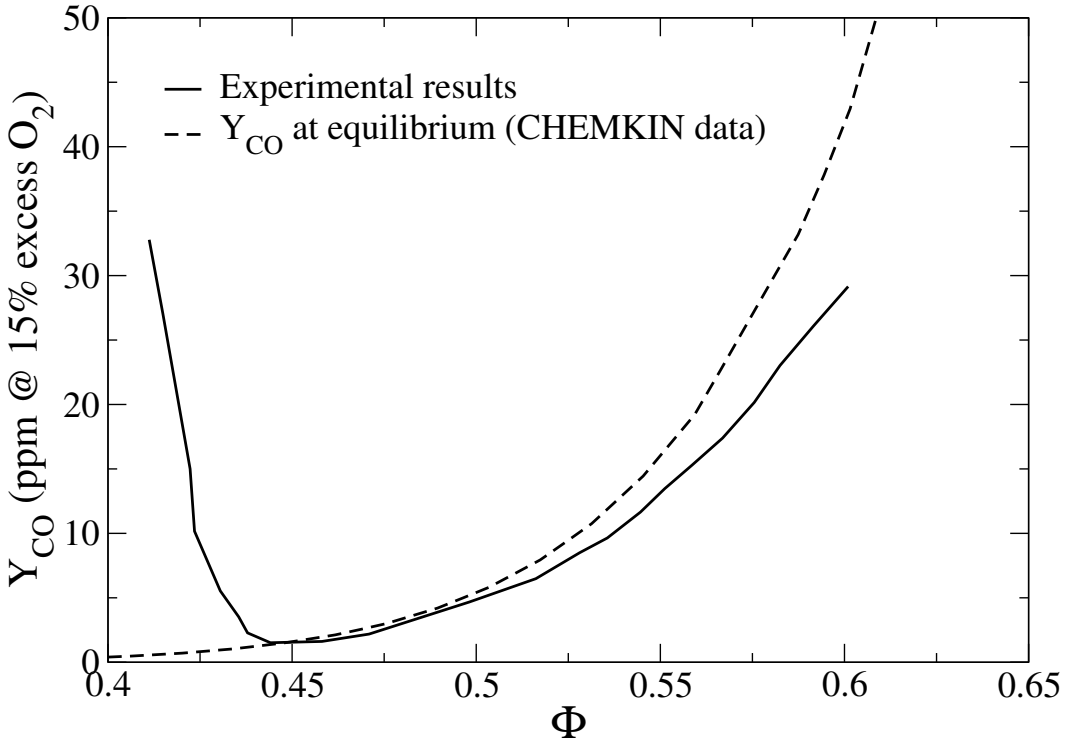

Figure 8: Equilibrium CO mass fraction (in ppm @ 15 percent excess O_2) value compared with experimental CO emission measurements. For Φ>0.44, the CO levels are close to the equilibrium value predicted by the library.

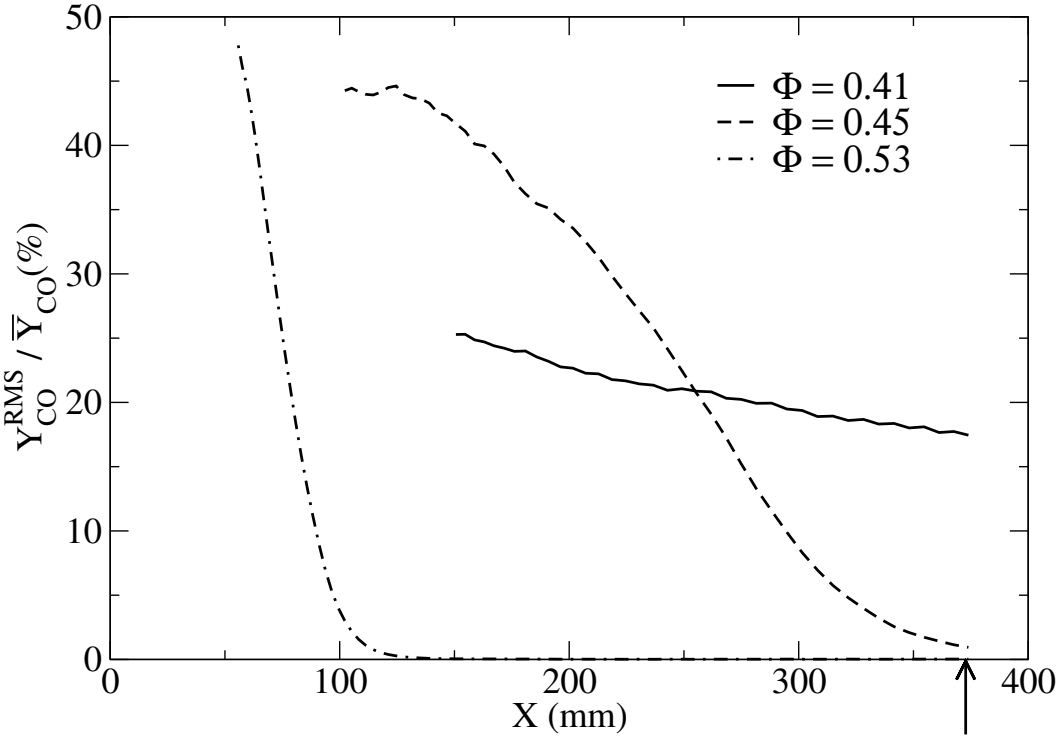

Figure 9: Normalized CO mass fraction fluctuations RMS ($Y_{CO,RMS}/\overline{Y_{CO}}$) as a function of the axial distance from the dump plane for different equivalence ratio. Only the region beginning downstream two flame length downstream from the dump plane is shown. The location of the emission probe is shown by an arrow.

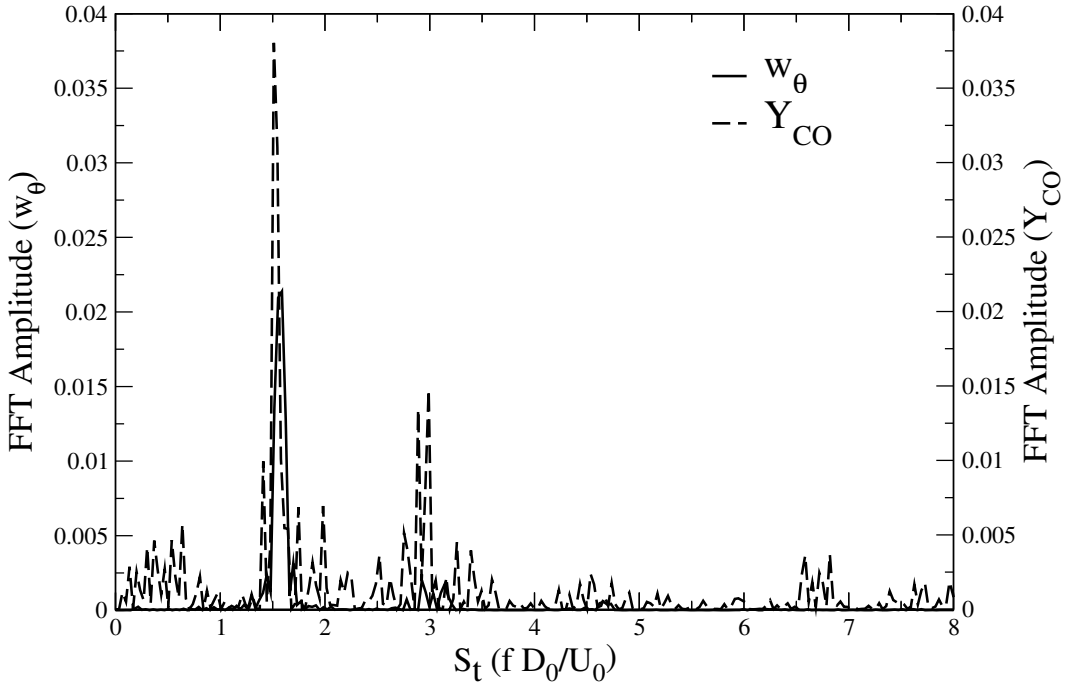

Figure 10: CO mass fraction (Y_{CO}) and vorticity (w_Θ) fluctuation spectra for Φ=0.41

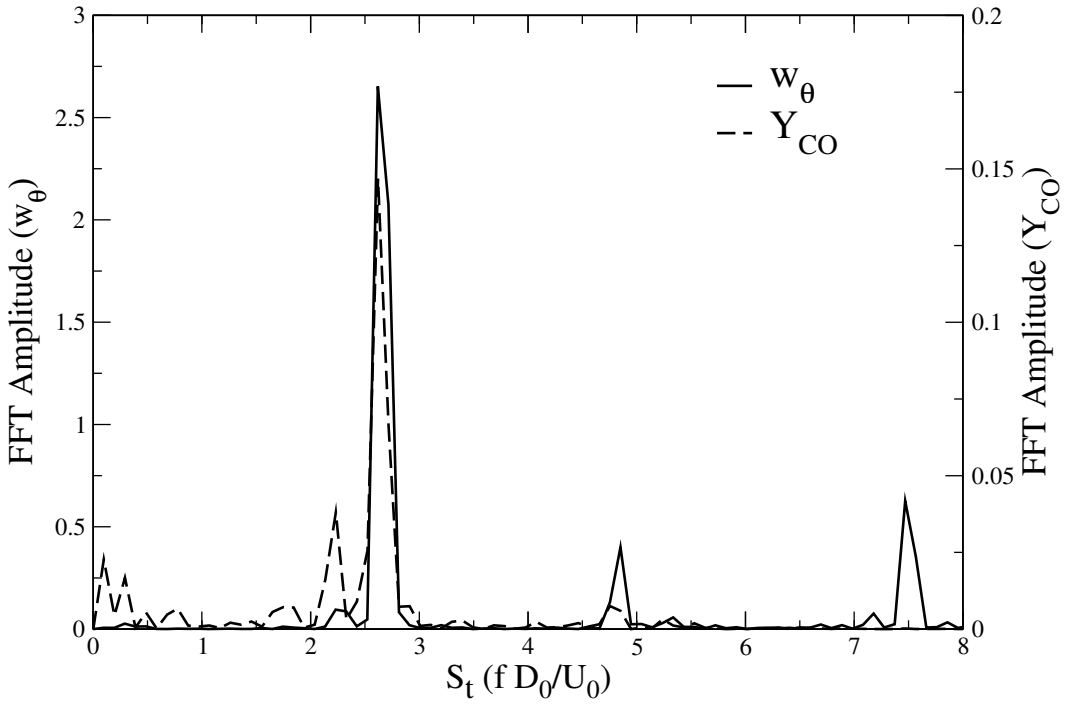

Figure 11: CO mass fraction (Y_{CO}) and vorticity (w_Θ) fluctuation spectra for Φ=0.53

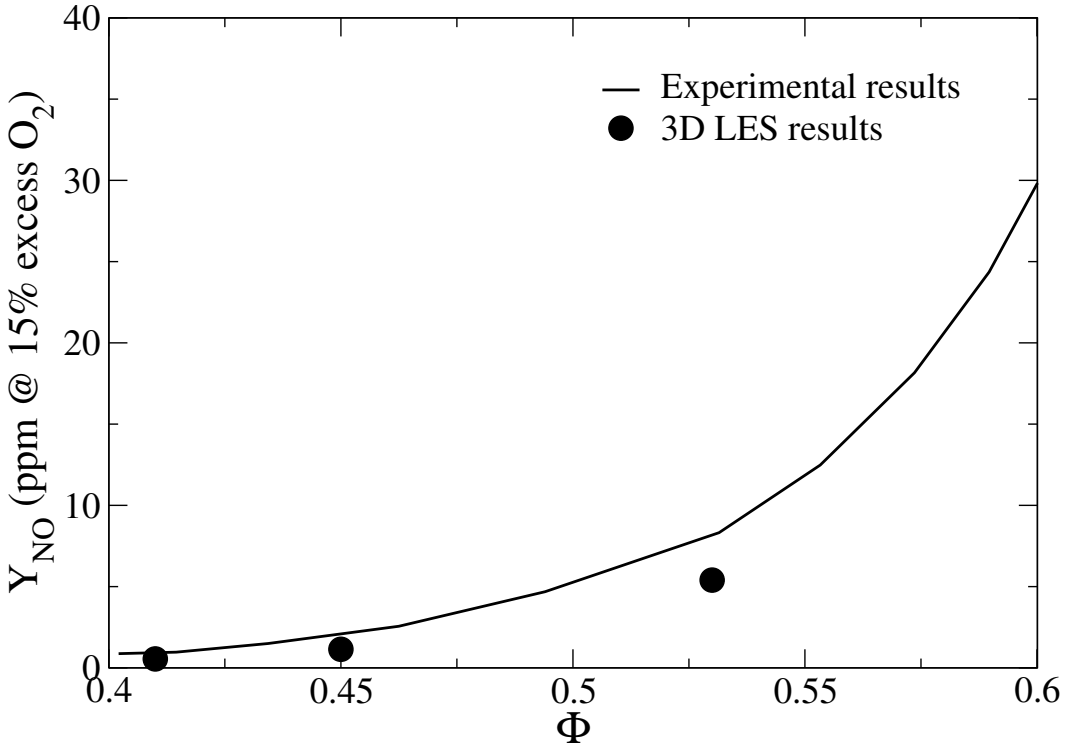

Figure 12: NO mass fraction (in ppm @ 15 percent excess O_2) from experimental data and 3D computations vs. equivalence ratio.

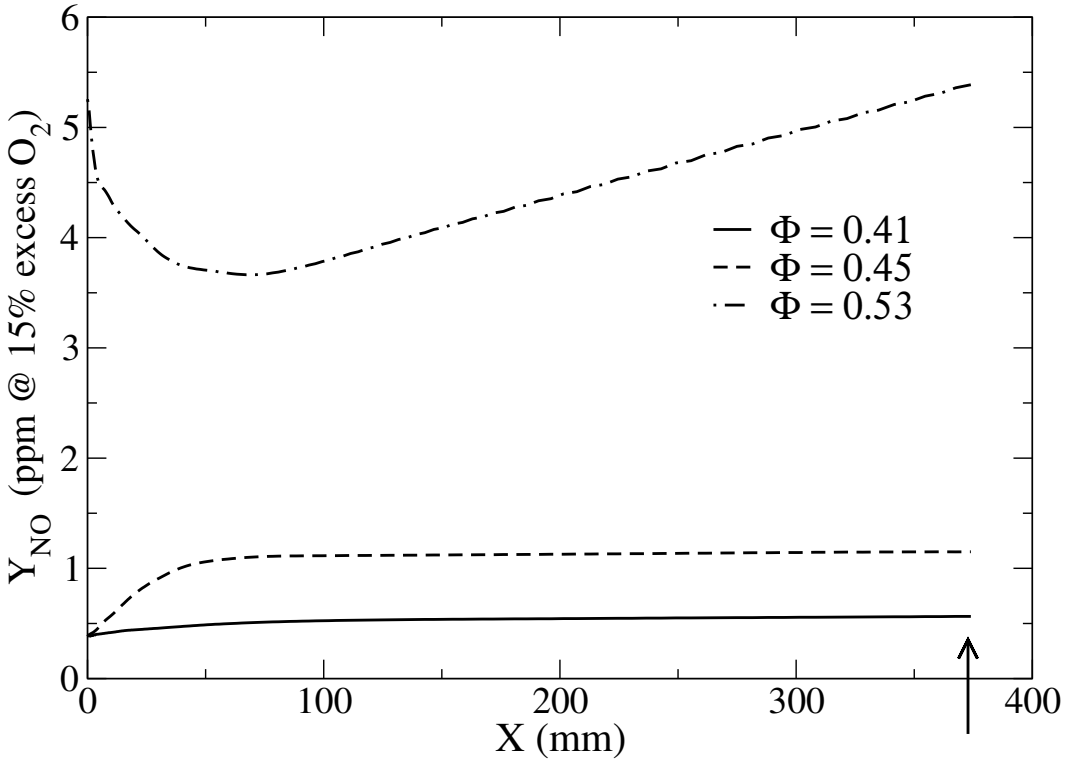

Figure 13: NO mass fraction (in ppm @ 15 percent excess O_2) as a function of the axial distance from the dump plane for different equivalence ratios. The location of the emission probe is shown by an arrow.

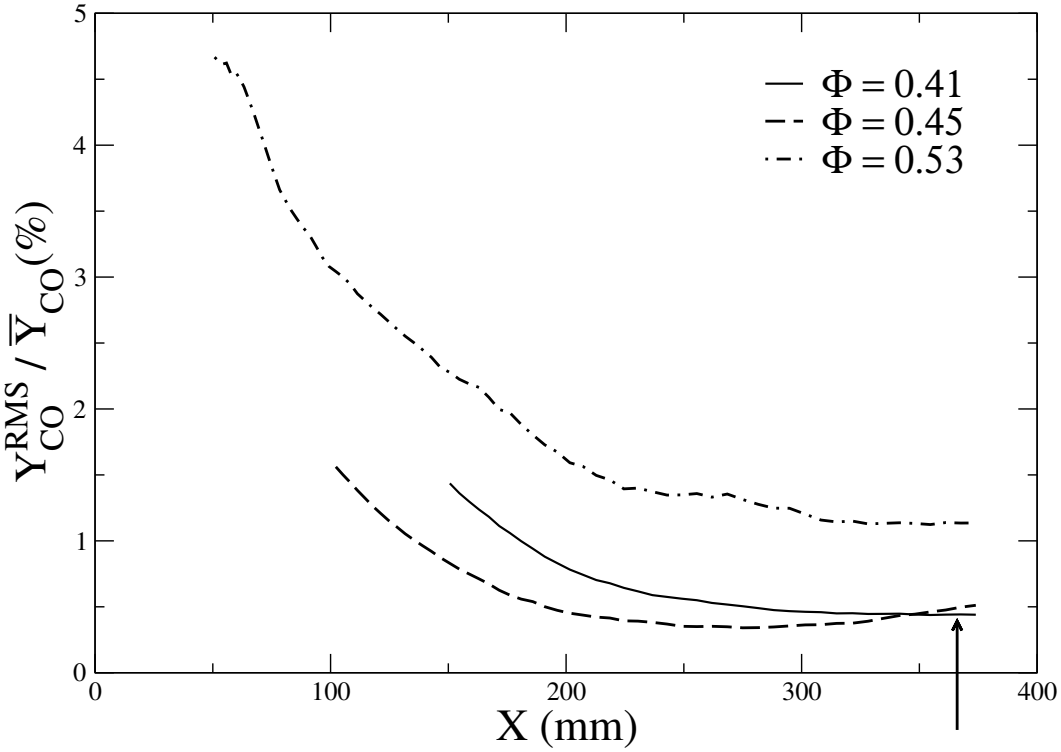

Figure 14: Normalized NO mass fraction fluctuations RMS ($Y_{NO,RMS}/\overline{Y_{NO}}$) as a function of the axial distance from the dump plane for different equivalence ratios. Only the region beginning two flame length downstream from the dump plane is shown. The location of the emission probe is shown by an arrow.